Wind and fetch dependence of gas transfer velocity in an Arctic sea-ice lead determined from eddy covariance CO flux measurements

John Prytherch[1] and Margaret J Yelland[2]

[1]Stockholm University
[2]National Oceanography Centre, Southampton

November 21, 2022

Abstract

The air-water exchange of trace gases such as CO is usually parameterized in terms of a gas transfer velocity, which can be derived from direct measurements of the air-sea gas flux. The transfer velocity of poorly soluble gases is driven by near-surface ocean turbulence, which may be enhanced or suppressed by the presence of sea ice. A lack of measurements means that air-sea fluxes in polar regions, where the oceanic sink of CO is not well known, are generally estimated using open-ocean transfer velocities scaled by ice fraction. Here, we describe direct determinations of the CO gas transfer velocity from eddy covariance flux measurements at a sea-ice lead during the summer-autumn transition in the central Arctic Ocean. CO uptake by the lead water is determined using flux footprint analysis of water-atmosphere and ice-atmosphere flux measurements made under conditions (low humidity and high CO signal) that minimise errors due to humidity cross-talk. The mean gas transfer velocity over the lead is found to have a quadratic dependence on wind speed:

$= 0.189$

which is 25 to 30% lower than commonly used open-ocean parameterizations. As such, current estimates of polar ocean carbon uptake are likely to overestimate gas exchange rates in typical summertime conditions of weak convective turbulence. The gas transfer velocities also exhibit a dependence on the dimension of the lead, via its impact on fetch length and hence sea state. Scaling transfer velocity parameterizations for regional gas exchange estimates will therefore require incorporating lead width data.

Hosted file

`agusupporting-information.docx` available at https://authorea.com/users/530557/articles/597388-wind-and-fetch-dependence-of-gas-transfer-velocity-in-an-arctic-sea-ice-lead-determined-from-eddy-covariance-co-flux-measurements

Wind and fetch dependence of gas transfer velocity in an Arctic sea-ice lead determined from eddy covariance CO_2 flux measurements

J. Prytherch[1], M. J. Yelland[2]

[1]Department of Meteorology, Stockholm University, Stockholm, Sweden.

[2]Marine Physics and Ocean Climate, National Oceanography Centre, Southampton, UK.

Corresponding author: J. Prytherch (john.prytherch@misu.su.se)

Key Points:

- CO_2 uptake in lead waters is determined using flux footprint analysis of water-atmosphere and ice-atmosphere flux measurements
- The wind-speed dependent gas transfer velocity in the lead is suppressed by 25-30 % relative to the open ocean
- k exhibits a dependence on fetch, implying estimates of polar ocean carbon uptake should incorporate lead width data

Abstract

The air-water exchange of trace gases such as CO_2 is usually parameterized in terms of a gas transfer velocity, which can be derived from direct measurements of the air-sea gas flux. The transfer velocity of poorly soluble gases is driven by near-surface ocean turbulence, which may be enhanced or suppressed by the presence of sea ice. A lack of measurements means that air-sea fluxes in polar regions, where the oceanic sink of CO_2 is not well known, are generally estimated using open-ocean transfer velocities scaled by ice fraction. Here, we describe direct determinations of the CO_2 gas transfer velocity from eddy covariance flux measurements at a sea-ice lead during the summer-autumn transition in the central Arctic Ocean. CO_2 uptake by the lead water is determined using flux footprint analysis of water-atmosphere and ice-atmosphere flux measurements made under conditions (low humidity and high CO_2 signal) that minimise errors due to humidity cross-talk. The mean gas transfer velocity over the lead is found to have a quadratic dependence on wind speed:

$$k_{660} = 0.189\ U_{10}^{2}$$

which is 25 to 30% lower than commonly used open-ocean parameterizations. As such, current estimates of polar ocean carbon uptake are likely to overestimate gas exchange rates in typical summertime conditions of weak convective turbulence. The gas transfer velocities also exhibit a dependence on the dimension of the lead, via its impact on fetch length and hence sea state. Scaling transfer velocity parameterizations for regional gas exchange estimates will therefore require incorporating lead width data.

Plain Language Summary

Polar oceans absorb large amounts of carbon dioxide from the atmosphere, but there is a lot of uncertainty over exactly how much is taken up. The amount the oceans absorb depends on both the concentration of carbon dioxide in the water, and the rate of gas exchange between the ocean and the atmosphere. This rate itself depends mostly on wind speed. In sea ice-regions, which even in winter have some areas of open water, the gas exchange rate is often estimated by using an ocean gas exchange rate, multiplied by the fraction of the sea-ice area that is open water. However, there are very few measurements of the gas exchange rate in sea-ice areas, and there is an on-going debate about whether the sea ice itself increases or decreases the exchange rate. Here, direct measurements of the gas exchange rate were made in an area of water surrounded by sea ice in the Arctic during summer and the beginning of autumn. The measured gas exchange rate was lower than typical ocean rates, and depended on both the wind speed and the size of the open water area that the wind had blown across. This finding suggests that the absorption of carbon dioxide by polar oceans has previously been overestimated, and that to make better estimates we will need to include information on the size of open water areas within sea ice.

1 Introduction

Polar oceans are important to the global ocean-atmosphere carbon cycle as major sinks. The Arctic Ocean accounts for approximately 3% of global ocean area, and is estimated to have 5-14% of the net global ocean carbon uptake, e.g.: 66 to 199 Tg (Tg = 10^{12} g) C $year^{-1}$(Bates & Mathis, 2009); 166 ± 60 Tg C $year^{-1}$ (MacGilchrist et al., 2014); 180 ± 130 Tg C $year^{-1}$ (Yasunaka et al., 2018). The net Southern Ocean carbon flux is likely smaller

due to the balance of strong summer uptake with strong winter emissions, but sparse sampling results in large uncertainty: Uptake for oceans south of 50˚S (14% of the global ocean surface area) was estimated as 50 Tg C $year^{-1}$ (Takahashi et al., 2009), while a more recent estimate for waters south of 60˚S was approximately 130 Tg C $year^{-1}$ (Woolf et al., 2019).

Most estimates of polar ocean carbon uptake utilise collations of ship and buoy observations of the partial pressure of CO_2 in seawater, pCO_2w, such as the Surface Ocean CO_2 Atlas (SOCAT) version 4 (Bakker et al., 2016). For sea-ice areas, air-sea flux estimates derived from pCO_2w observations are scaled by the fraction of open water within the sea-ice area, either linearly (e.g. Takahashi et al., 2009; Bates and Mathis, 2009) or by incorporating a parameterization that estimates a flux larger than that from a linear scaling with open water fraction due to physical forcings from the sea ice itself (Yasunaka et al., 2018).

For a poorly soluble trace gas such as CO_2, the flux across an air-water interface, F_c, is often represented as a product of the air-water fugacity or partial-pressure difference, ΔpCO_2; the aqueous-phase solubility of the gas, $K0$; and the transfer coefficient, or transfer velocity, k:

$$F_c = k\, K0\, \Delta pCO_2 \qquad (1)$$

The transfer velocity represents the interfacial turbulent processes on the water side that control the rate of exchange and that are challenging to measure directly (e.g., Jähne et al., 1987; Wanninkhof et al., 2009). Gas transfer velocity is thus typically parameterized using more easily measurable variables, most commonly wind speed. Despite recent progress, the greatest source of uncertainty in determining the carbon uptake by the global oceans remains the uncertainty in the form (quadratic or cubic) of the gas transfer parameterization (Woolf et al., 2019). Over the ocean, the most widely used parameterizations have a quadratic dependence on wind speed (e.g. Wanninkhof et al., 2014, hereafter W14; Nightingale et al., 2000; Ho et al., 2006) but there remains uncertainty in determining k, both at low and moderate wind speeds due to the suppression of near-surface turbulence by surfactants (e.g. Salter et al., 2011), and at higher wind speeds due to the uncertain influence of bubble-mediated exchange and wave forcing (e.g. McGillis et al., 2001; Woolf, 2005). Some progress has been made incorporating sea state into gas transfer parameterizations but there remain significant challenges due to limited data and an incomplete understanding of the physical mechanisms involved (Blomquist et al., 2017; Brumer et al., 2017).

Over lakes, indirect estimates of gas transfer velocity from dual tracer experiments determined lower wind-speed dependence than for the open ocean (Wanninkhof, 1992; Cole & Caraco, 1998; MacIntyre et al., 2010). Convection-driven turbulent mixing resulting from surface buoyancy flux has been observed to enhance gas transfer in lakes (MacIntyre et al., 2010): in small lakes (< 10 ha) at latitudes < 60º, it was determined to be the dominant driver of gas transfer (Read et al., 2012). The gas transfer velocity has also been found to depend on both the size and shape of the lakes (Vachon & Prairie, 2013).

In sea-ice regions there remains uncertainty in air-water gas transfer rates due to both lack of measurements and the influence of the sea ice itself on near-surface turbulence. Ship-based determinations of k using direct eddy covariance (EC) flux measurements in the Arctic (Prytherch et al., 2017) and Antarctic (Butterworth & Miller, 2016a) marginal ice zones and pack ice found an approximately linear scaling of k with open water fraction. Observations from acoustic Doppler profile instruments mounted on floating drifters close to sea ice have shown suppressed near-surface turbulent dissipation rates, a proxy for turbulent mixing, relative to open ocean measurements, presumably due to attenuation of the wave field by the

sea ice (Zippel & Thomson, 2016). Early estimates of *k* using radon isotope-deficit showed, in ice concentrations greater than 70%, an enhancement of *k* above that expected from a linear scaling with open water fraction (Fanning and Torres, 1991). Subsequent experiments using this method have shown both suppressions (Rutgers van der Loeff et al., 2014) and enhancements (Loose et al., 2017) of *k* relative to a linear scaling. The *k* estimates reported by Loose et al. (2017) showed only a weak dependence on wind speed, and the authors surmised that other kinetics were driving the gas exchange within the marginal ice zone and pack ice. Such forcing has been hypothesised to result from a number of physical mechanisms impacting the interfacial mixing, including shear between floating ice and the underlying water and form drag on the wind from ice edges (Loose et al., 2014), conclusions supported by laboratory measurements (Loose et al., 2009; Lovely et al., 2015). For low ice concentrations (< 60%) and moderate ice drift velocity (ice/wind velocity ratio > 0.02), this additional forcing is predicted to be larger than any suppression of gas transfer resulting from wave field attenuation, whilst for higher ice concentrations or lower ice drift velocity, the gas transfer suppression is equal to or greater than the enhancement, resulting in a linear or lower scaling with open water fraction (Bigdeli et al., 2018).

Sea ice itself is known to be permeable to salt and gases via brine channels (Gosink et al., 1976) and drives physical and biogeochemical processes such as carbonate crystal formation and brine exclusion that affect CO_2 concentrations in the underlying water (e.g. Miller et al., 2011a). Ice-atmosphere fluxes may make a large contribution to the net carbon flux in polar regions (Delille et al., 2014). Varying CO_2 partial pressure in brines is thought to explain the range of sea ice-atmosphere CO_2 fluxes observed in both spring-summer (Geilfus et al., 2012, 2015; Nomura et al., 2013; Delille et al., 2014; Sievers et al., 2015) and winter seasons (Miller et al., 2011b). The observed flux is primarily dependent on the surface temperature (Delille et al., 2014; Geilfus et al., 2012) and on the snow conditions. Snow cover is generally shown to reduce the flux (e.g. Geilfus et al., 2012), with snow depth greater than 9 cm observed to block exchange (Nomura et al., 2010) and superimposed ice layers reduce or even entirely block the flux (Geilfus et al., 2012, 2015). On summer sea ice, there can also be a large flux into melt ponds due to the undersaturation of CO_2 in the melt waters. This flux is typically short lived (<~ 1week) as the shallow melt waters rapidly equilibrate with the atmosphere following their formation, though ongoing melt can maintain a smaller undersaturation (Geilfus et al., 2015).

EC measurement of trace gas flux, combined with measurement of air and water gas concentrations and solubility enables *k* to be directly determined on time scales of order 30 min and spatial scales on the order of 100 m to 1 km. Whilst EC CO_2 flux measurement has been long-established in terrestrial settings, they have proved challenging in marine conditions because of the typically much smaller CO_2 flux and the difficult measurement environment. Recent developments in instrumentation and measurement techniques, particularly the use of air-drying to reduce the water vapor cross-sensitivity apparent in infrared absorption-based CO_2 measurements (e.g. Miller et al., 2010; Blomquist et al., 2014) have improved agreement between *k* determined from EC and from other methods.

There is a well known (see e.g. the summary by Butterworth & Else, 2018) disparity in the magnitude of sea ice-atmosphere CO_2 fluxes as observed by enclosure or chamber-based methods (Miller et al., 2015) and EC. The flux measured using chamber-based techniques is typically in the range -5 to +2 mmol m^{-2} day^{-1} (here a positive flux value represents a flux from the surface to the atmosphere; Geilfus et al., 2012, 2015; Nomura et al., 2010, 2013; Delille et al., 2014) whereas the flux determined from EC has a much larger range and variability, with magnitudes often in excess of 50 mmol m^{-2} day^{-1} (e.g. Else et al., 2011; Miller et al., 2011; Sievers et al., 2015). This may result from the relatively low

sensitivity and cold temperature biases (Burba et al., 2008) of the open-path EC instrumentation (Butterworth & Else, 2018). More recent EC measurements using closed path instrumentation reported fluxes of 1.75 ± 5 mmol m^{-2} day^{-1} from snow-covered ice, in broad agreement with chamber flux measurements made close by (Sievers et al., 2015). EC flux measurements using a closed path system with airstream drying also measured low fluxes, averaging -0.03 mmol m^{-2} day^{-1} in spring with full ice cover, and -2.9 mmol m^{-2} day^{-1} during the summer ice breakup when the surface was a mixture of water and ice (Butterworth & Else, 2018). In contrast, measurements during the spring season from collocated open-path instruments measured fluxes several orders of magnitude higher.

Here we report direct determination of gas transfer velocities in an open lead close to the North Pole during summer and autumn in 2018. The gas transfer velocity is determined from EC measurement of CO_2 fluxes between both the lead waters and atmosphere, and between the sea-ice surface and atmosphere, using a flux footprint analysis. The dependence of the gas transfer velocity on wind speed, fetch and buoyancy is determined and the implications discussed.

2 Materials and Methods

2.1 Expedition

The Arctic Ocean 2018 expedition was focused on Arctic clouds, the sources of cloud condensation nuclei and ice nucleating particles in the central Arctic Ocean, and the interactions of clouds and sea ice. The expedition, based on the icebreaker *Oden*, departed Longyearbyen on August 1 2018 and transited north into the ice pack. On August 13, *Oden* moored to an ice floe at 89.6ºN 40ºE. The ice floe was approximately 0.8 km × 1.5 km in size, and surrounded by dense pack ice as well as some lead systems. Instrumentation was deployed on the ice floe at several different locations for a period of four weeks. *Oden* drifted with the ice floe, occasionally repositioning with changing wind direction to maintain winds onto the bow for the purposes of measurements made onboard the ship. The ice camp lasted until late on September 14 2019, when *Oden* departed the ice floe at 88.49ºN 36.8ºE, returning to Longyearbyen on September 20 (Figure 1a). In addition to the measurements made on the ice floe, a wide variety of atmospheric and oceanographic measurements were made onboard *Oden* during both the ice camp and the transits.

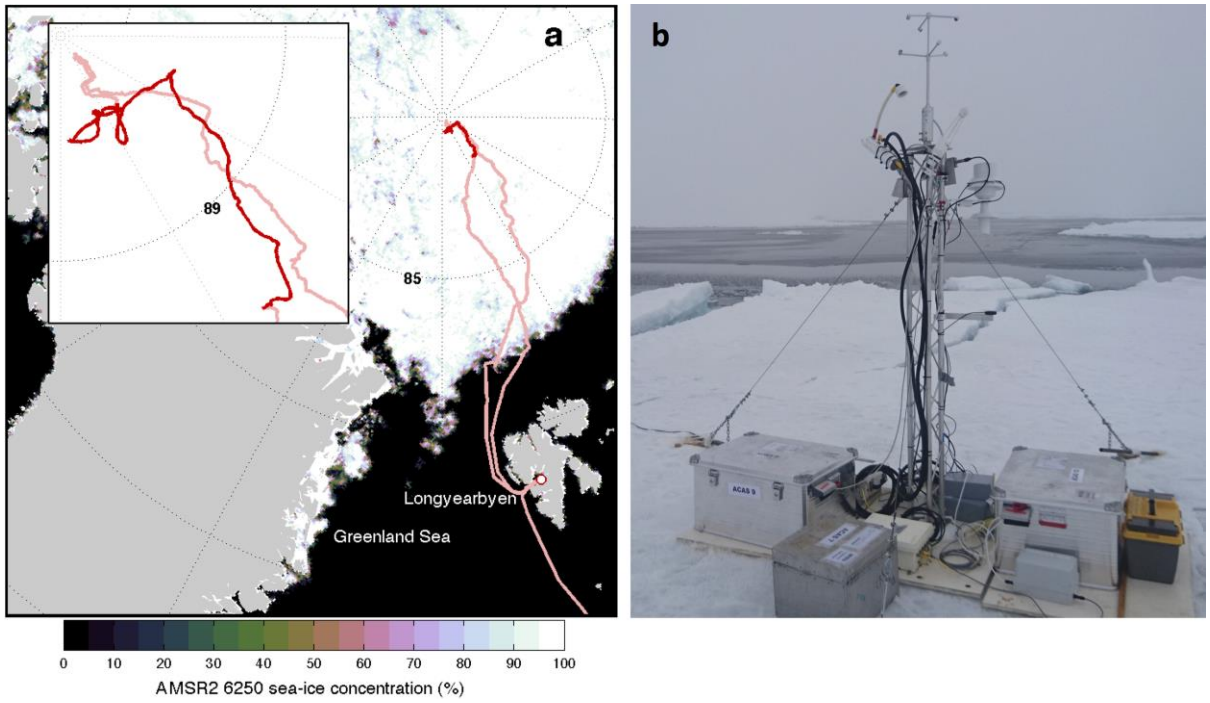

Figure 1. a) Arctic Ocean 2018 expedition track, with the ice camp portion of the expedition highlighted (darker red). Sea-ice concentration (AMSR2 6250 satellite passive microwave measurement, Spreen et al., 2008; ASI 5 sea-ice algorithm) is shown for September 1, 2018. b) The open lead mast on August 18, 2018. The surface water pCO_2w sensor is positioned approximately 3 m out into the lead to the left of frame.

2.2 Open lead mast

A measurement site was located adjacent to a large lead system. This open lead site was on the far side of the ice floe from *Oden's* mooring, approximately 1.5 km distant from

the ship. Instrumentation at this site was primarily concerned with processes occurring within, at or above the surface of the lead water. A small hut (approximately 3 m × 3 m × 2 m) was constructed for storage and shelter and serves as a reference point in the moving sea-ice environment. A 2 m high meteorological mast (Figure 1b) was installed on August 16, approximately 140 m from the hut and most of the other measurement systems and approximately 6 m from the ice edge at the lead.

The three-dimensional wind vector and sonic temperature was measured with a METEK uSonic-3 heated sonic anemometer. Density of CO_2 and H_2O as well as air pressure were measured by both a LI-COR 7200 closed-path infrared gas analyzer (IRGA) and a LI-COR 7500 open-path IRGA. The closed-path IRGA derives dry air mole fractions from the density measurements using internal measurements of temperature and humidity. This instrumentation all measured at 20 Hz. The measurement volume of the uSonic-3 was at a height of 2.55 m above the ice surface, with the inlet for the closed-path IRGA 0.25 m below the anemometer, and the measurement volume of the open-path IRGA 0.45 m below the anemometer.

Also positioned on the mast were a Heitronics KT15.IIP infrared temperature sensor. The measurement point was focused on lead water approximately 5 m from the ice edge closest to the mast. The sensor measures *Ts*, the skin temperature of the water or ice. An aspirated temperature and humidity sensor measured air temperature (*Ta*) and relative humidity (*RH*) at a height above the ice of 2 m. A GPS unit at the mast determined location and ice drift velocity. A Pro Oceanus CO_2-Pro CV membrane equilibration sensor was deployed beneath a float in the lead waters closest to the mast approximately 3 m from the ice edge and at 0.5 m depth, measuring pCO_2w, the partial pressure of CO_2 in seawater. The CO_2-Pro CV was removed on September 9 due to heavy ice formation at its location.

Restrictions imposed to facilitate aerosol measurements onboard *Oden* and on the ice floe meant that all power at the open lead site came from batteries. The meteorological mast instrumentation was powered by six 12V batteries, which were exchanged on a daily basis. Data were logged at the mast, and backups taken daily. The mast was in operation for 28 days from August 16 to September 12, when the last data backup was taken at 20:00 UTC. In the early hours of September 13, moving ice destroyed the mast and the equipment installed there.

2.3 Data processing

2.3.1 Meteorology and fluxes

The fast response (20 Hz) measurements are divided into flux periods of 30-minutes duration. For each flux period, a double rotation is used to rotate the winds into the streamline (Wilczak et al., 2001). The momentum flux τ, and friction velocity u_* are determined from the covariance of the fluctuations of the horizontal along-, cross- (u', v') and vertical-wind (w') components as:

$$u_* = \left(\tau/\rho\right)^{1/2} = \left(\overline{u'w'}^2 + \overline{v'w'}^2\right)^{1/4} \quad (2)$$

where ρ is the mean air density, ' indicates a fluctuation from the mean value, and an overbar indicates a mean. The mean wind speed, U is adjusted to a height of 10 m using a log profile

$$U_{10} = U + u_* \log\left(10/z_u\right)/\kappa \quad (3)$$

where z_u is the wind measurement height (2.55 m) and κ is the von Karman constant (here set as 0.4). In the summer conditions that comprise the majority of the data here, the air and surface temperatures are similar, and applying a stability adjustment (Andreas et al., 2010) to the U_{10} values results in a mean absolute change of approximately 1%. There is uncertainty in the applicability of similarity-theory based stability corrections in heterogeneous sea-ice regions (e.g. Lupkes et al., 2012). Hence in the following results we use U_{10} without an additional stability adjustment. Following linear detrending of the time series for each flux period, the kinematic flux, F_x of a scalar quantity x is determined as:

$$F_x = \overline{x'w'} \quad (4)$$

and the cospectra C_{xw} is determined from the same measurements. For CO_2, the flux is calculated from c, the dry mole fraction of CO_2 measured by the closed-path IRGA with units of ppm m s^{-1}. The dynamic flux (units of mmols m^{-2} day^{-1}) is determined using ρ_a, the dry air density and the molecular weight. The sensible heat flux is determined from the sonic temperature, t_{son} following correction for side wind path lengthening (van Dijk et al., 2004). Humidity is corrected for in the sensible heat flux calculation using a bulk estimate of the latent heat flux (Smith, 1988) following Persson et al. (2005). Fast response H_2O density measurements from the open-path IRGA are corrected for density effects (Webb et al., 1980) on a point-by-point basis following Miller et al. (2010; 2004). The resulting humidity mixing ratio is used to determine the latent heat flux, F_l. Throughout the analysis here we use the convention that a positive flux is upwards, i.e. from the water surface to the overlying air.

Calculation of flux detection limits for the CO2 flux measurements is described in supplementary material section S1. Determination of measurement time lag, and correction of high frequency signal attenuation in the closed-path IRGA measurements is described in supplementary material section S2.

For the duration that the open lead mast was in operation, the necessary input measurements were available to allow 1206 30-minute CO_2 flux measurements from the closed-path IRGA. Standard statistical tests for skewness, kurtosis (Vickers and Mahrt, 1997) and stationarity (Foken and Wichura, 1996) were applied to assess the suitability of the measurements for flux calculation. The statistical tests were failed by approximately 37 % of the flux measurements and these were removed, leaving 754 fluxes for analysis.

2.3.2 Atmospheric and waterside pCO_2

The CO_2 dry mole fraction measurements from the closed-path IRGA were converted to pCO_2a using measurements of temperature, humidity and pressure made on the mast, and the measurements averaged to the 30-minute flux measurement time. Waterside CO_2 was measured at a depth of 0.5 m in the open lead using the CO_2-Pro CV membrane equilibration instrument. The sensor was factory calibrated from 0 to 600 ppm CO_2 prior to deployment, with a manufacturer-specified accuracy of 0.5%. The instrument sampled the seawater directly using a Sea-Bird Scientific SBE 5P submersible pump and measures the mole

fraction of CO_2 in moist air in equilibration with the sampled water. The mole fraction is converted to CO_2 partial pressure (pCO_2w) using the sensor's measurement of gas stream pressure. The water – air partial pressure difference is then calculated directly.

2.3.3 Lead dimensions and flux footprint

Both the ice floe and the lead were dynamic. The combined system moved and rotated with the surrounding ice pack. For ease of reference, a local coordinate system, 'loc' is defined, with the mast located at the origin and the open lead hut located 137 m N^{loc} of the mast. The open lead was generally located from NNE^{loc} clockwise around to SWW^{loc} of the mast The open lead varied in shape and size significantly during the measurement period (Figure 2a), depending on the meteorological conditions and the movement of the surrounding ice pack. The spatial dimensions of the lead were determined using a hand-held laser range finder (Naturalife PF4). Measurements were taken of the distance to the near and far shores of the lead, from a position adjacent to the mast at radial intervals of approximately 22.5˚. Lead dimension measurements were attempted twice daily during the period of mast operation. Measurement was not always possible, for example when precipitating particles prevented an accurate laser reading. Error in determining the lead dimensions results primarily from interpolation of the ice edge between the measurements, error in the positioning of the laser relative to the mast, and error in determining the edge of the lead. Measurement error due to the positioning of the ranger is estimated as ± 0.5 m. The laser signal is poorly reflected by water, which can lead to a possible bias in the determined dimensions. Measurement error in determining the edge of the lead is estimated as underestimation of up to 10% in near shore distances, and overestimation of up to 10% in far shore distances. The distance of the lead far shores varied from approximately 50 m to > 450 m, and was generally greatest in the SW^{loc} and S^{loc} directions.

Fetch for each flux measurement was determined from the distance between the near and far shores in the mean wind direction. The spatial dimensions of the surface area contributing to the flux, and the relative contribution of locations within that area, i.e. the flux footprint, was calculated using a two-dimensional model (Kljun et al., 2015). The model takes the mean meteorological conditions as inputs. For each flux measurement, the footprint was rotated into the mean wind direction and the nearest-in-time lead dimensions were used to determine the relative proportions of the footprint over water and over ice (Figure 2a). An open water fraction, *owf*, is defined as the proportion of the flux footprint that occurs over the lead water surface.

The *owf* can be used to partition the measured CO_2 flux, $F_{c,m}$, into the contribution through the water surface $F_{c,ow}$, and that through the ice / snow surface $F_{c,ice}$ (Loose et al., 2014; Prytherch et al., 2017):

$$F_{c,m} = \left(1 - owf\right) F_{c,ice} + owf\, F_{c,ow} \qquad (5)$$

At the open lead site, melt ponds were only present during the first week of measurements, when the flux footprint was almost entirely over the lead (Section 3.1). As such, we omit an additional term from equation (5) for fluxes through melt pond surfaces (Prytherch et al., 2017).

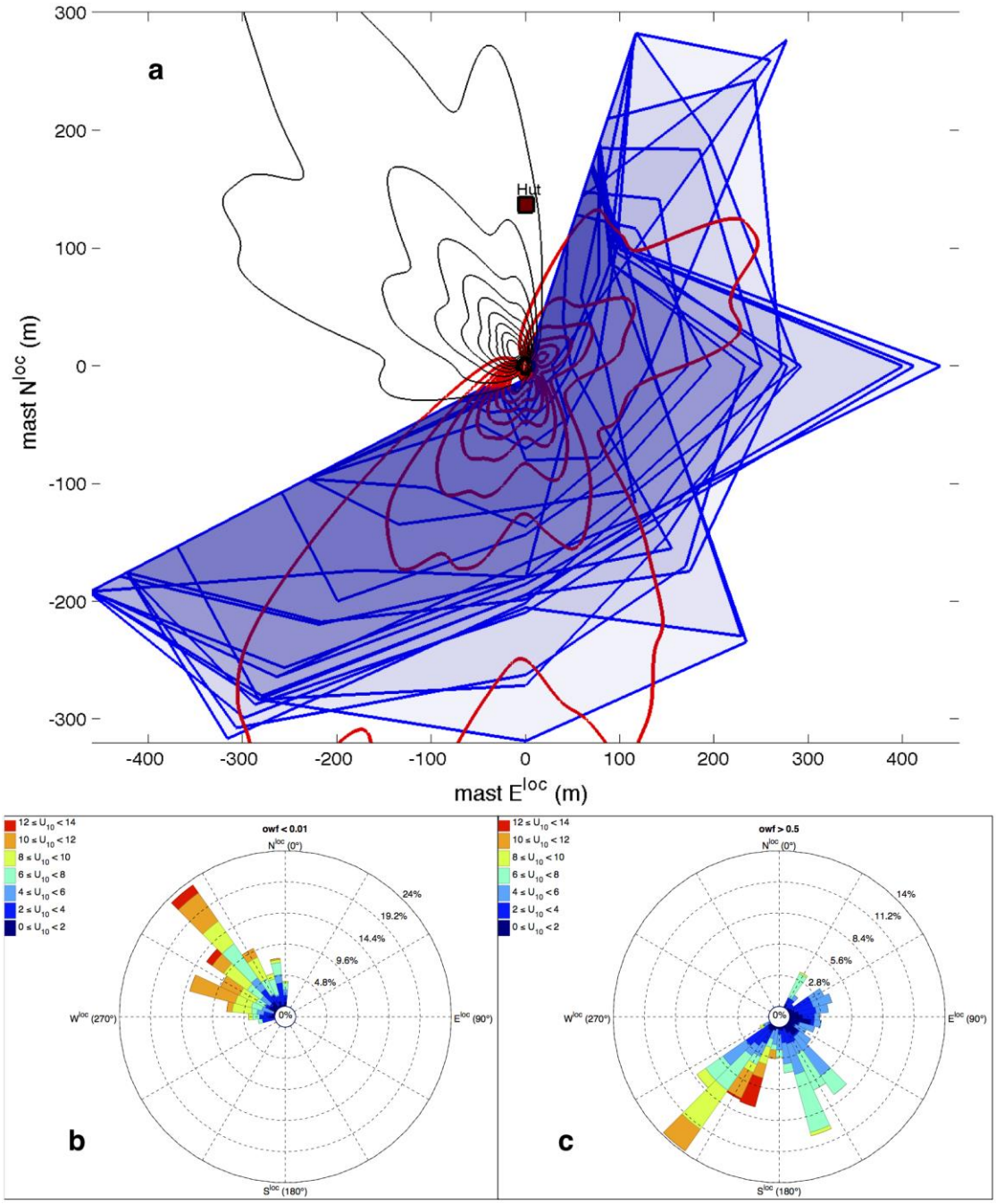

Figure 2. a) Open lead dimensions and flux footprint climatology estimates shown in mast-relative coordinates, with the mast located at 0 N^{loc}, 0 E^{loc}. The lead edges (blue lines) were determined on a near-daily frequency. Shading indicates the relative proportion of experiment time that a location was open water. Contours indicate footprint climatology flux contributions for the duration of the experiment in steps of 10% from 10 to 90%, for *owf* > 0.5 (red) and *owf* < 0.01 (black). Lower plots are windroses of 30-minute average 10-metre wind speeds and directions for b) measurements with *owf* < 0.01 and c) measurements with *owf* > 0.5. Directions are in the local frame of reference, direction widths are 10º, color indicates wind speed range and radius shows the fractional contribution to the set of winds shown.

312

313 2.3.4 Gas transfer velocity

314 The gas transfer velocity through the water surface is determined from $F_{c,\,ow}$ using the
315 normalized form of equation (1):

$$k_{660,ow} = \left(F_{c,ow} \Big/ \left[K0\,\Delta pCO_2\right]\right)\left(Sc/660\right)^{1/2} \quad (6)$$

316

317 where $k_{660,\,ow}$ is the measured gas transfer velocity normalized to a Schmidt number (*Sc*) of
318 660 to account for the temperature dependence of seawater molecular diffusivity and
319 viscosity (W14). The temperature used to determine *Sc* is the lead surface temperature
320 determined by the KT15.IIp radiometer. The radiometer measurement is first corrected for
321 sky reflection using an empirically-derived correction (Hignett, 1998) and downwelling
322 short- and long-wave radiation measurements made using gymbal-mounted Eppley
323 Laboratory PSP and PIR radiometers onboard *Oden*. The solubility, *K0*, is determined
324 following Weiss (1974) from the lead's surface temperature, and from salinity as measured
325 continuously at 1 Hz by a Seabird TSG sampling from *Oden's* pumped underway line that
326 draws from a depth of 8 m. There were 628 k_{660} measurements with all necessary inputs
327 derived from flux measurements that passed the statistical tests.

328 If $F_{c,\,ice}$ is known or can be estimated, then $F_{c,\,ow}$ can be determined from the measured CO_2
329 flux using equation (5). For the analysis here, a minimum *owf* criteria of 0.5 was set, resulting
330 in 383 $F_{c,\,ow}$ measurements. and 359 $k_{660,\,ow}$ measurements available for analysis. A higher
331 criteria reduces the number of measurements available for analysis, whilst a lower criteria
332 decreases the sensitivity of the measurement (section S1), demonstrated with the correlation
333 of quadratic least squares regressions of $k_{660,\,ow}$ to U_{10}. Scaling the fluxes by *owf* also requires
334 that the flux detection limit be scaled. An *owf* limit of 0.5 doubles the flux uncertainty for a
335 given ΔpCO_2 and U_{10}, all else being equal (Figure S1). For the closed-path IRGA sensitivity
336 determined empirically here, a U_{10} of 8 m s^{-1}, $|\Delta pCO_2|$ of 86 μatm (≈ 88 ppm) and *owf* of 0.5
337 gives an individual flux uncertainty of approximately 25%. For a wind speed of 2 m s^{-1}, the
338 individual flux uncertainty is approximately 66%. For the open-path, the corresponding
339 individual flux uncertainties are 105% and 266%. Fluxes are defined as over ice/snow
340 surfaces ($F_{c,\,ice}$) if *owf* < 0.01, a criteria met by 280 F_c measurements. For fluxes with *owf*
341 between 0.5 and 0.01 (91 F_c measurements, 12% of the total) the measured flux may contain
342 significant contributions from both water and ice surfaces. As such, we do not analyze these
343 measurements further.

344 2.4 Density perturbations and Water vapor cross-sensitivity

345 A well-known issue for EC measurements of mass fluxes determined from density
346 measurements is that they must be corrected for perturbations caused by heat and pressure
347 (Webb et al., 1980). The closed-path IRGA measures H_2O and CO_2 density, and determines
348 dry mole fractions from these in real-time using measurements of temperature, pressure and
349 humidity made inside the infrared measurement cell. The mole fractions are then converted to
350 mixing ratios. The corrections for density (Webb et al., 1980) are performed for the open-
351 path IRGA in post-processing on a point-by-point basis following Miller et al. (2004, 2010)
352 using t_{son} and pressure measured in the IRGA interface box. Temperature equilibration in the
353 sample inlet reduces the magnitude of the sensible heat correction for closed path
354 measurements. The colocation of the temperature pressure and humidity measurements in the

IRGA measurement cell enables the density correction for the closed-path IRGA to be more precise than for the open path, and partly explains the greater sensitivity of this system (Section S1).

Measurement of CO_2 by absorption-based sensors such as IRGAs is directly affected by spectral cross-talk from the H_2O signal (e.g. Blomquist et al., 2014). This spectral interference results in a cross-sensitivity to water vapor in the CO_2 signal. This cross-talk has presented a significant obstacle to CO_2 flux measurement, particularly in environments such as the open ocean with relatively large H_2O fluxes and small CO_2 fluxes (Prytherch et al., 2010; Miller et al., 2010; Landwehr et al., 2014). A now widely-accepted approach is to dry the airstream prior to measurement, e.g. with an inline Nafion membrane drier (Miller et al., 2010; Blomquist et al., 2014).

The moisture-flux dependent error in F_c was characterized by Blomquist et al. (2014) as a cross-talk error proportionality coefficient, μ. From field and laboratory experiments, Blomquist et al. determined that for a closed-path LI-COR 7200 IRGA, μ = 0.1 ppm kg g^{-1}. For their field measurements in the equatorial Indian Ocean (mean latent heat flux, F_l = 100 W m^{-2}, equivalent to a specific humidity flux of approximately 0.0343 g kg^{-1} ms^{-1}; small CO_2 flux resulting from small ΔpCO_2 and light winds), the humidity cross talk error in F_c from an undried-airstream closed-path IRGA was more than 7 times the magnitude of the flux measured with a dried-airstream closed-path IRGA. Both F_l and F_c were positive (upwards) and correcting for the cross-talk error acts to reduce the measured F_c. When conditions are more suited to CO_2 flux measurement, airstream drying may not be required. For example closed-path IRGAs sampling from either dried or non-dried airstreams were shown to measure similar F_c when F_l was less than 7 W m^{-2} (Landwehr et al., 2014; Honkanen et al., 2018).

For the measurements reported here, It was not possible to deploy a drying system due in part to power (and hence pump) limitations at the measurement site. Measurement of F_c without airstream drying was possible because the humidity flux was very small and ΔpCO_2 relatively large. The mean absolute F_l measured with the open-path IRGA was 4.5 W m^{-2} (≈ 0.0014 g kg^{-1} m s^{-1}). The F_l measured by the closed-path was lower, 0.6 W m^{-2} (≈ 1.8 10^{-4} g kg^{-1} m s^{-1}) (Figure 3h). The closed path humidity flux measurement is not corrected for high frequency spectral attenuation, which is observed to be much higher (> 1 order of magnitude) than the equivalent signal loss for CO_2 (e.g. Yang et al., 2016; Butterworth & Miller, 2016b). Here, the open-path IRGA is preferred for the determination of F_l, but the cross-talk error in F_c measured by the closed-path IRGA is dependent on F_l as measured in that system. For the lead water flux measurements, the low humidity flux, combined with a large CO_2 signal driven by the persistent large ΔpCO_2 in the open lead (mean ≈ -85 µatm; section 3.1) resulted in an average humidity cross-talk correction in the closed-path IRGA F_c of ~ 1%. The direction of F_c was downwards, opposite to F_l, and hence the humidity cross-talk correction acts to increase the measured F_c. It was not possible to apply the frequency-dependent cross-correlation approach to correcting water vapor cross-sensitivity (Edson et al., 2011; Blomquist et al., 2014) due to the small heat fluxes and the lack of another independent scalar flux measurement.

3 Results

3.1 Meteorology

For the first 14 days of measurements (August 17 to 10:00 August 31), the wind measured at the mast was mostly flowing over the lead waters. Following this open water period, the wind measured at the mast was mostly flowing over ice until the end of measurements at 20:00 September 12. Wind speeds at the open lead site were generally moderate (30-minute average U_{10} 6.0 m s^{-1}) with several periods of higher winds, and a maximum 30-minute U_{10} of 13.1 m s^{-1} (Figure 3a). Higher winds were generally from NW^{loc} and SW^{loc} directions (Figure 2b). For the open water period, the highest winds were from the SW^{loc} with some moderate winds from SSE^{loc} (Figure 2c).

Air and surface temperature were typically 0 to -2˚C during the open water period, typical for the sea-ice melt season. After this date temperatures dropped to around -4˚C before rising again to near freezing on September 3, then decreasing sharply around September 6. Surface freezing is determined by the complete surface energy balance. For the observations here, the surface energy balance followed the surface temperatures and the onset of the autumn freeze up (determined following Tjernström et al. 2012) was estimated as August 28. Conditions remained variable following the onset of freeze up and the passage of storm systems led to higher winds and marked increases in temperatures.

For the open water period the surface temperature of the lead waters varied between 0˚C and the freezing point of approximately -1.7˚C (Figure 3b). Prior to August 31 there are occasional periods with lead temperatures lower than the freezing point, likely associated either with initial ice formation or drifting sea ice entering the infrared radiometers target area. The pCO_2w sensor was removed September 9 14:00 due to increasing ice build up, and the majority of the lead became frozen over around September 10.

During the measurement period examined here pCO_2a was 394.1 ± 2.6 µatm (uncertainties are given as ± *s.d*, the sample standard deviation, unless otherwise stated), and pCO_2w 307.9 ± 4.6 µatm. The mean ΔpCO_2 was -85.4 ± 4.7 µatm. Throughout the measurement period the ΔpCO_2 shows a general slow decrease from decreasing pCO_2w (Figure 3c), presumably due to primary production within the lead. This slow decrease is marked by two periods (around August 22 and August 29) of sharp increase in pCO_2w following periods of higher winds and the resulting increase in mixing, gas transfer and the resulting increased equilibration of the lead waters with the atmospheric CO_2.

Sea-ice drift velocity at the mast site during the measurement period, determined from GPS measurement, was 0.12 ± 0.08 m s^{-1}. Sea-ice surfaces in the vicinity of the mast were generally covered with snow. Snow depth surveys over the ice floe on September 7 and September 14 determined median snow depths of 8.6 ± 7.4 cm and 10.6 ± 4.2 cm respectively. Cumulative snow depth measurements from an automated snow buoy deployed in the center of the ice floe on August 27 determined ~2 cm snow accumulating between buoy deployment and the end of the ice camp in mid-September. Melt ponds were present on the ice floe at the beginning of the lead measurement period, though there were none in the immediate vicinity (within 50 m) of the mast. For this period the majority of the flux footprint was over water. From around August 24 to the end of measurements, a period which includes nearly all the over-ice flux measurements, melt ponds surfaces were frozen and increasingly snow covered.

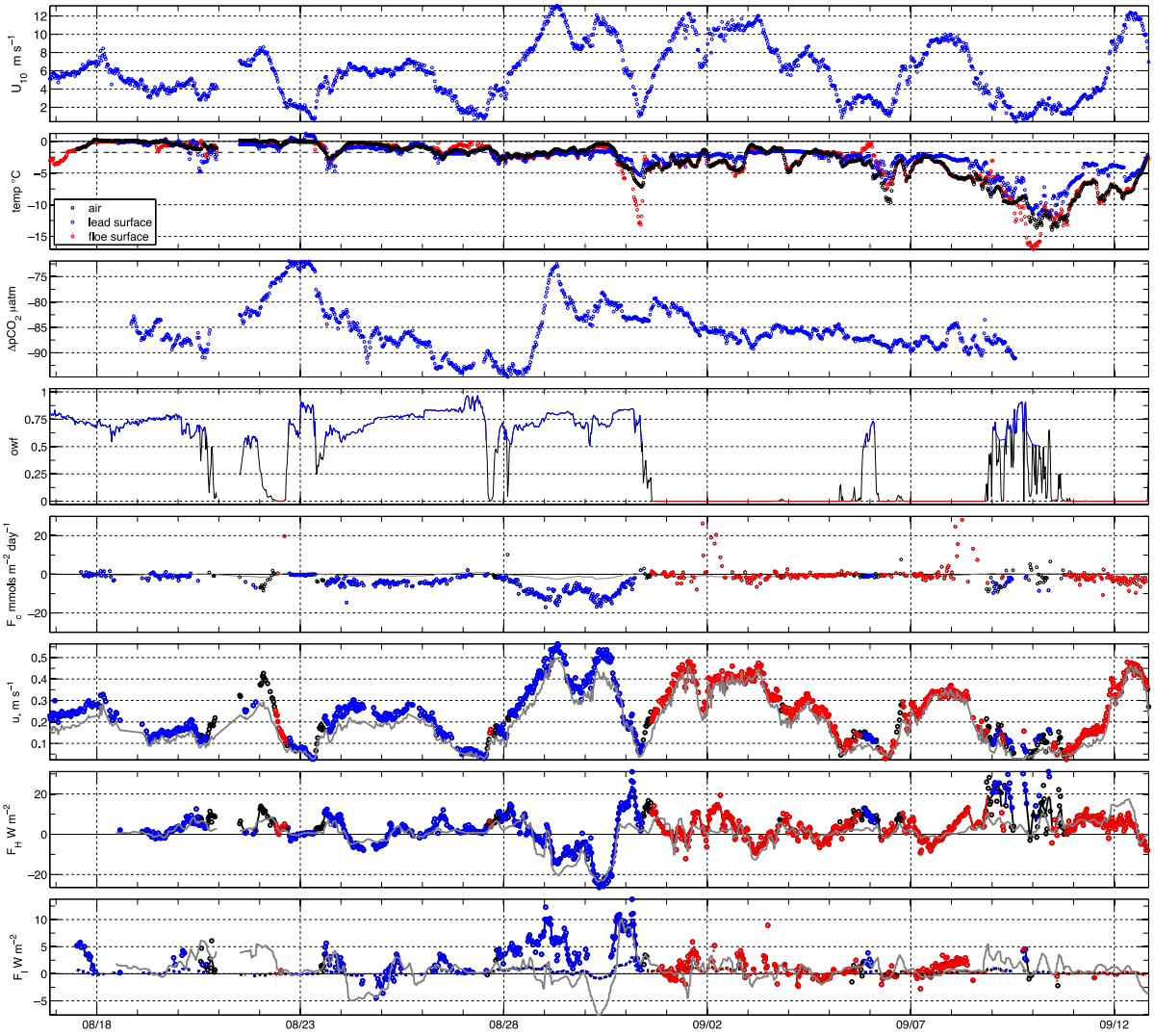

Figure 3. Time series from the open lead site for the period of closed-path IRGA F_c measurement. All measurements are 30-minute averages or fluxes. a) Wind speed. b) Temperature of air (black), the lead surface determined by KT15 IR sensor (blue) and ice surface determined by KT15 IR sensor mounted on *Oden* (red). The dashed line is the freezing point of surface seawater. c) Water – air pCO_2 difference, determined using the CO_2-Pro CV sensor and atmospheric concentration from either the trace gas system onboard *Oden* (red) or the closed path IRGA at the open lead (blue). d) Open water flux footprint fraction *owf*. Blue indicates *owf* > 0.5, red indicates *owf* < 0.01. e) Flux of CO_2 , $F_{c,\,m}$, measured by closed-path IRGA. $F_{c,\,icemod}$ is shown as a grey line. f) Friction velocity. g) Sensible heat flux. h) Latent heat flux determined by the open-path IRGA. The closed-path IRGA latent heat flux measurements are shown as dashed lines. For e through h color indicates *owf* as in d. In f, g and h, the grey lines are the model estimates of Smith (1988).

3.2 Heat and momentum flux

Friction velocity measurements (Figure 3f) are slightly higher than a bulk relationship (Smith, 1988), and the difference is greater for measurements determined with $owf > 0.5$. This may be due to increased drag from the lead edges. Normalized momentum flux cospectra (shown for $U_{10} > 4$ m s^{-1}) have a similar form for measurements over both ice and water surfaces (Figure 4), and agree with the theoretical form determined for measurements over uniform terrestrial surfaces with neutral stability (Kaimal et al., 1972). Ogive forms of the cospectra asymptote to 0 and 1 at low and high frequencies respectively, indicating that the full range of turbulent frequencies is measured.

EC sensible heat fluxes are small, typically less than 20 W m^{-2} (Figure 3g). Sonic temperature cospectra agree broadly with the theoretical neutral Kaimal form for measurements over water and ice. EC latent heat flux determined with the open-path IRGA is also small, generally < 5 W m^{-2} with the exception of the period August 29 to August 31, when fluxes are up to ~10 W m^{-2} (Figure 3h). Despite the small flux magnitude, over water the latent heat flux cospectra (Figure 4) approximate the theoretical neutral Kaimal form, except at low frequencies, where the averaged cospectra are approximately zero below a normalized wave number of 0.002. Over ice, the latent heat fluxes have substantial noise at the lower frequencies. A more detailed analysis of the heat and momentum fluxes will be the subject of a subsequent manuscript.

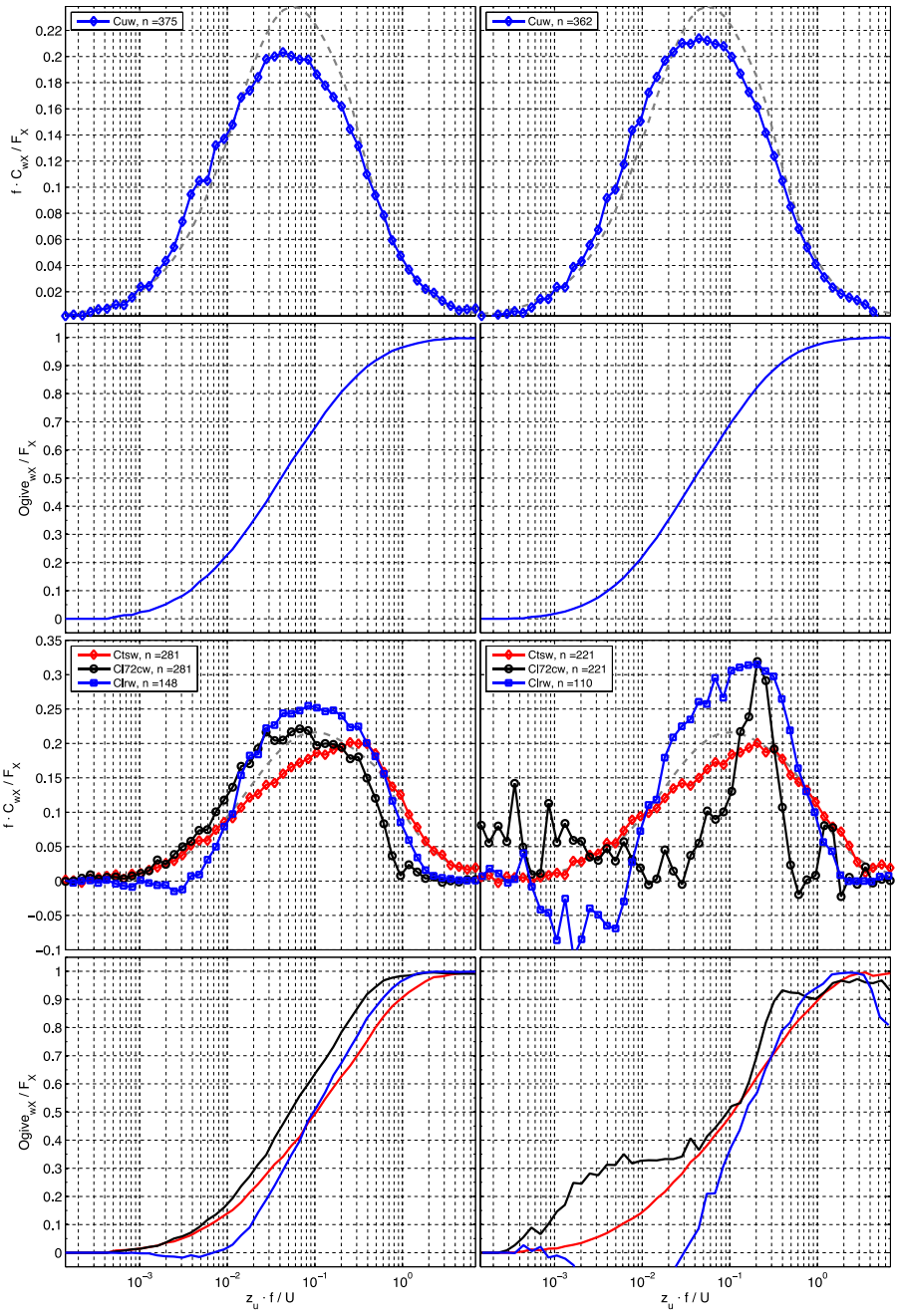

Figure 4. Normalized, frequency weighted cospectra and ogives for flux measurements from the lead mast at U_{10} > 4 m s^{-1}. a) Momentum flux cospectra for *owf* > 0.5. b) Momentum flux cospectra for *owf* < 0.01. c) Ogive for the data shown in a. d) Ogive for the data shown in b. e) Scalar flux cospectra of sonic temperature (red), latent heat (blue) and CO_2 (black) for *owf* > 0.5. f) As for e for *owf* < 0.01. g) Ogive for the data shown in e. h) Ogive for the data shown in f. All cospectra are normalized by flux and frequency prior to averaging. Ogives are normalized by flux prior to averaging. Frequency in all panels is represented as a dimensionless wavenumber, $z_u f / U$, where f is measurement frequency.

3.3 ice / snow – atmosphere CO_2 flux

For the periods when $F_{c,\,ice}$ was determined (*owf* < 0.01; Figure 3e) winds were almost entirely from the NW^{loc} (Figures 2 and 8a). In general the measured $F_{c,\,ice}$ are relatively small (median -4.3 ± 4.2 mmols m^{-2} day^{-1}). For low wind periods with U_{10} < 5 m s^{-1}, the median flux was –1.3 mmol m^{-2} day^{-1}. The variability in the individual measurements (*s.d* for these periods was 1.9 mmol m^{-2} day^{-1}) results in some upwards fluxes, with a maximum upwards flux of +2.2 mmol m^{-2} day^{-1}. For the periods September 1 12:00 to September 2 12:00 and September 7 18:00 to September 9 00:00, the over-ice F_c are larger and much more variable (median 5.9 ± 21.2 mmols m^{-2} day^{-1}) with the maximum magnitude F_c +62.6 mmols m^{-2} day^{-1} (not shown). The sensible heat flux measurements (Figure 3g) are also higher than the bulk estimate for these two periods. There were relatively high off-ice winds during these two periods (mean 30-minute U_{10} 8.7 ± 2.2 m s^{-1}), and *Oden* was directly upwind of the open lead mast, which may have lead to contamination of the measurements from *Oden's* emissions, though this was not apparent in the pCO_2a measurement. The high fluxes do not persist during the sustained higher off-ice winds from September 2 12:00 to September 3 12:00 and do not occur during the high winds on September 12. *Oden* was not upwind for these periods. The high ice/snow-surface fluxes may also result from wind-driven pressure pumping (e.g., Takagi et al., 2005; Bowling & Massman, 2011), a process poorly understood in snow over sea ice due in part to the inability of chamber-based measurements to determine wind-forced fluxes.

With the two anomalous periods excluded, the $F_{c,\,ice}$ measurements were less variable with a small median downward flux (-0.7 ± 1.3 mmols m^{-2} day^{-1}) and a maximum magnitude of -6.5 mmols m^{-2} day^{-1}. The winds for these fluxes were slightly lower (U_{10} 7.5 ± 2.8 m s^{-1}). These flux values are of similar magnitude to those observed for snow-covered sea ice during winter, spring and early summer using chamber-based measurements (Delille et al., 2014; Geilfus et al., 2012, 2015; Nomura et al., 2010, 2013, 2018) and closed-path eddy covariance (Sievers et al., 2015; Butterworth & Else, 2018). These are the first reported measurements of sea-ice-atmosphere CO_2 flux obtained in the late summer and fall freeze up periods that we are aware of.

The $F_{c,\,ice}$ measurements exhibit a weak relationship with ice surface temperature (as determined for the snow and ice surface adjacent to *Oden's* mooring). The relationship, with larger downwards fluxes at higher temperatures and fluxes close to zero when temperatures fall to -5ºC or less, is similar to one observed for CO_2 flux over Antarctic sea ice (Delille et al., 2014) but highly scattered with poor correlation (Figure 5a; linear least squares fit r = 0.19). The poor correlation in these measurements may result from the spatial separation between the flux and ice temperature measurements. The fluxes at warmer temperatures are smaller than those observed by Delille et al. (2014), possibly due to different snow coverage. The ice fluxes have a stronger wind-speed dependence (Figure 5b; linear least squares fit r = 0.44), which may indicate high wind speed ventilation of the snow cover (Takagi et al., 2005). In the absence of available snow depth observations within the flux footprint, a multiple linear regression model of $F_{c,\,ice}$ with $T_{s,\,ice}$ and U_{10} is determined ($F_{c,\,icemod} = 1.31 + 0.11 \times T_{s,\,ice} - 0.34 \times U_{10} - 0.037 \times T_{s,\,ice} \times U_{10}$; fit r = 0.48. Figure 3e).

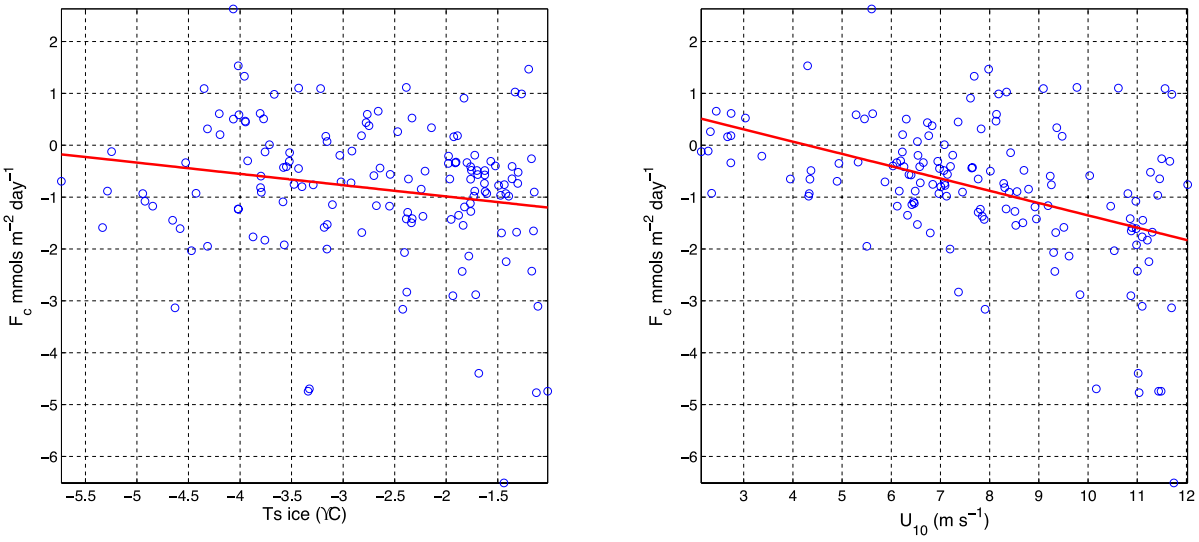

Figure 5. Relationship of $F_{c,\,ice}$ to a) *Ts* and b) U_{10}. Measurements are shown excluding the high flux periods between September 1 12:00 and September 2 12:00, and between September 7 18:00 and September 9 00:00. A linear least squares regression is shown for each data set (a, r = 0.19. b, r = 0.44).

3.4 water – atmosphere CO_2 flux

$F_{c,\,ow}$ can be determined from equation (5) using $F_{c,\,icemod}$. For $F_{c,\,ow}$ with $owf > 0.5$, the flux direction was almost always downwards in the direction driven by the ΔpCO_2 gradient. The over-water CO_2 fluxes showed a strong relationship with wind speed. The wind-speed dependence is particularly noticeable in the period August 28 to 31, with 30-minute average U_{10} up to 13.1 m s^{-1} (mean 9.4 ± 2.2 m s^{-1}) and a maximum F_c into the water of 22.4 mmols m^{-2} day^{-1} (median -12.4 ± 4.5 mmols m^{-2} day^{-1}). Accounting for the ice flux measurements in the determination of $F_{c,\,ow}$, as compared with disregarding them (i.e. with setting $F_{c,\,icemod} = 0$ in equation (5)), acts to reduce the magnitude of $F_{c,\,ow}$ by an average of 0.22 ± 0.32 mmols m^{-2} day^{-1}, with a maximum reduction of 1.2 mmols m^{-2} day^{-1}. For measurements at $U_{10} > 10$ m s^{-1}, the average reduction in $F_{c,\,ow}$ from accounting for the ice flux is 0.64 ± 0.20 mmols m^{-2} day^{-1}.

For $F_{c,\,ow}$ with $owf > 0.5$, the majority of the measurements were obtained from NE^{loc}, SSE^{loc}, and SW^{loc} wind directions, and the fluxes measured at higher winds ($U_{10} > 8$ m s^{-1}) were entirely from the SW^{loc} direction (Figure 2c). The open lead was sometimes very large in this direction, with a fetch greater than 300 m (Figure 2a). The climatology of $owf > 0.5$ flux footprints shows that for fluxes from the SW^{loc} direction, the footprint region that lies over an ice surface is mostly the near region between the mast and the lead to the immediate SW^{loc} of the mast. Cospectra of $F_{c,\,ow}$ have the expected form, allowing for the high frequency tube attenuation effect (Section S2), and are similar to the other scalar fluxes (Figure 4). The $F_{c,\,ice}$ cospectra are much noisier, with greater than expected low frequency signal, resulting from the much smaller signal in these measurements. The majority of the signal remains at the expected frequencies, peaking at a normalized wavenumber of 0.3.

3.4 Gas transfer velocity

Gas transfer measurements binned by wind speed (1 m s^{-1} width bins), have an approximately quadratic dependence on wind speed (Figure 6). The two highest bins, centered on U_{10} of 12.6 and 13.1 m s^{-1}, fall below this dependence and measurements at wind speeds > 12 m s^{-1} were excluded from the following fit determination. Reasons for this exclusion are discussed in Section 4. A quadratic fit is determined from least squares regression:

$$k_{660} = 0.189\,U_{10}^2 \quad (r^2 = 0.70) \qquad (7)$$

The gas transfer relationship to wind speed determined here is slightly weaker than that in commonly used models of gas transfer derived for open ocean measurements: The ratio of the relationship to that of W14 is 0.75; for the dual tracer-derived relationship of Nightingale et al. (2000) the ratio is 0.74 and for the EC-derived cubic wind speed-dependent relationship of McGillis et al. (2001) the ratio is 0.69. For wind speeds above 5 m s^{-1}, equation (7) is substantially higher (ratio of 1.30) than a relationship determined from dual tracer measurements frequently used to model gas transfer in lakes (Cole & Caraco, 1998). At lower wind speeds, equation (7) is lower than this relationship. Note that the dual tracer measurements used to derive this model were only made during low to moderate wind speed conditions and are extrapolated here for winds over 9 m s^{-1}. The measurements were also compared with a parametric model of gas exchange in sea ice regions (WAGT: Bigdeli et al., 2018; Loose et al., 2014). The WAGT model predicts the effective gas transfer velocity for a

given sea-ice concentration (SIC), k_{eff}, from inputs of wind and ice velocity, water and air temperature and SIC. Here, SIC of 50% and 90% are used to give a representative range and k_{660} is determined as $k_{660} = k_{eff} / (1\text{-SIC}/100)$. Compared with the measurements, the WAGT model over predicts for winds < 6 m s^{-1} and under predicts at higher wind speeds, despite the moderate ice drift velocity (the mean ratio of ice drift velocity to U_{10} was 0.018 ± 0.006).

Measurements at wind speeds above 12 m s^{-1} were excluded from the determination of least squares fit to the gas transfer velocity measurements (Figure 6). There are relatively few relatively few measurements (14) at these wind speeds. In addition, all the measurements were made during one period on August 29 with winds from an approximately constant wind direction ($200^{o\ loc}$), and with rapid variation in ΔpCO_2 (Figure 3) such that the measured value may not be representative of the pCO_2w within the flux footprint. Furthermore, in determining a wind-speed based relationship, data corresponding to the end points of the wind speed distribution may be subject to bias from two sources: firstly, uncertainty in the wind speed measurements. Secondly, the response time of the upper ocean, and the near-surface turbulence that drives the gas transfer, to changes in wind forcing. Both sources of error will cause measurements at the highest observed wind speeds to be biased low as the near surface turbulence at the measurement time has primarily been forced by winds of lower speeds. For the short fetch conditions measured here, the response time of the lead waters to changing wind forcing is expected to be less than 5 minutes (Aijaz et al., 2016) compared with timescales of 30 minutes to > 1.5 hours for the open ocean (Chen et al., 2016). As such the response time bias is likely to be small. If the measurements above 12 m s^{-1} are included, the resulting quadratic fit (exponent = 0.176) is lowered by 7% (Figure 6).

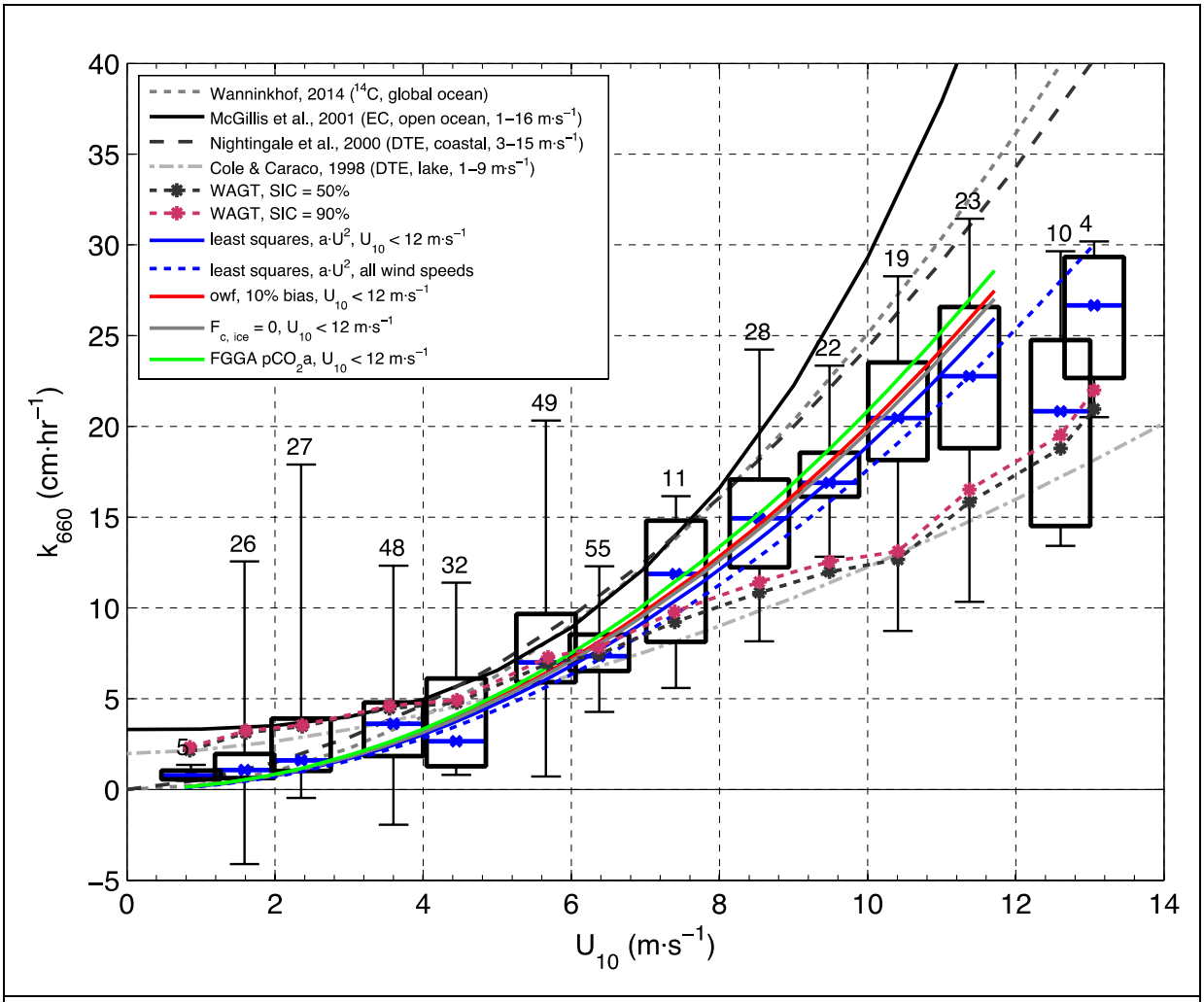

Figure 6. Observed relationship of k_{660} to U_{10} at the lead site. Gas transfer measurements, binned in 1 m s^{-1} wide wind speed bins, are shown as box and whisker plots (percentiles 2.5, 25, 50, 75, 97.5), and the number of measurements in each bin is indicated. Black and grey lines show published wind speed parameterizations of k_{660} as listed in the legend with the measurement type (radiocarbon inventory, ^{14}C; EC or dual-tracer experiment, DTE), location and wind speed range used to derive the parameterization. WAGT model predictions are shown for SIC of 50% and 90% (dotted lines and stars). Least squares quadratic fits are shown for data at U_{10} < 12 m s^{-1} (blue solid line); data at all wind speeds (blue dashed line); data at U_{10} < 12 m s^{-1} with a 10% reduction in measured lead far shore distance (red line); data at U_{10} < 12 m s^{-1} with $F_{c, ice}$ = 0 (grey line) and data at U_{10} < 12 m s^{-1} with pCO_2a from the *Oden* foremast FGGA sensor (green line).

4 Discussion

4.1 Potential sources of bias

Measurement of the relatively small ice-atmosphere fluxes represents a signal to noise challenge. For the sensitivity determined for the closed path sensor (Section S1 and Figure S1), and assuming a gas transfer relationship (W14), we can estimate the minimum flux magnitude required for measurement with 100% error as between 0.5 and 2.5 mmols m^2 day^{-}

[1], with higher flux magnitudes corresponding to higher winds. For the near ideal CO_2 measurement conditions reported here, the majority of the observed ice-atmosphere fluxes are within, or close to this somewhat arbitrary limit. An alternative approach is to set all Fc_{icemod} to 0 in the determination of F_w from equation (5). This increases the wind speed dependence of *k* slightly (Figure 6), with the ratio of the quadratic fit to the relationship of W14 increased from 0.75 to 0.78. It is notable that the sensitivity determined here for the closed-path IRGA is approximately four times greater than that determined for the open-path IRGA (Figure S1). The inability of open-path sensors to determine small fluxes such as those measured over ice surfaces here may explain the disparity between early eddy covariance and chamber-based measurements of ice-atmosphere CO_2 flux.

Biologically-derived surfactants, in particular soluble surfactants, are widely found in ocean surface microlayers at wind speeds up to at least 13 m s^{-1} (Sabbaghzadeh et al., 2017) and act to reduce gas transfer through suppression of capillary-gravity waves (McKenna & McGillis, 2004). The ubiquitous nature of surfactants means that the data from which existing *k* parameterizations are derived is very likely influenced by the presence of surfactants. Surface microlayer samples were obtained from the lead waters during the course of the ice camp using a variety of different measurement methods. Preliminary analysis has determined surfactant enrichment factors similar to open ocean values close to the ice edge, with enrichment decreasing for samples further out from ice edge (pers. comm., T-B Robinson, U. Oldernburg, Germany). This suggests that the observed gas transfer suppression is not the result of high surfactant enrichment.

In the calculation of ΔpCO_2, pCO_2a was obtained from the closed-path IRGA on the open-lead mast. Atmospheric CO_2 partial pressure was also determined using a Los Gatos Research (LGR) Fast Greenhouse Gas Analyzer (FGGA) gas onboard *Oden*, sampling air from an intake on *Oden's* foremast at 20 m above the surface (Prytherch et al., 2017). The FGGA determines CO_2 dry mole fraction at 10Hz from CO_2 absorption using internal cell pressure, temperature and water vapor measurements. Dry mole fractions were converted to pCO_2a using measurements of temperature, humidity and pressure made on the mast, and measurements averaged to the 30-minute flux measurement time. While it is located > 1 km horizontally away and ~18 m higher than the flux measurement location, this instrument has greater measurement accuracy than the closed-path IRGA and may provide a more reliable measurement of mean atmospheric CO_2 concentration. The range of pCO_2a measured by the LGR was 381 to 394 μatm, and the pCO_2a was lower than that measured by the closed-path IRGA by 7.5 ± 1.5 μatm. If the FGGA pCO_2a measurements are used in place of those from the IRGA to determine *k*, then the observed quadratic fit is higher, with a ratio of 0.83 relative to the relationship of W14.

The ice floe in the vicinity of the mast was relatively flat, with only low ridges and snow drift (< 20 cm height). Measurements of wind and air-sea exchange from platforms such as ships and buoys are biased by flow-distortion-induced errors (Yelland et al., 2002) which can be exacerbated by platform motion (Prytherch et al., 2015), but such biases are not expected to affect the measurements reported here.

The determination of both *owf* and fetch is dependent on lead dimension measurements. The challenging measurement environment and manpower availability resulted in both low spatial resolution (~ 22.5º) and low measurement frequency (~ daily), which will contribute to random error in the determination of the lead dimensions. In addition, there may be a bias resulting from the stronger laser return signal from ice edges and ridges, relative to water. This may result in a mean overestimation of the lead size,

particularly for measurement of the distance to the far shore. This bias was estimated as up to 10% of each range measurement. A set of *owf* and fetch measurements were determined assuming the maximum bias within this range (i.e., far-shore range measurements were reduced by 10%, and near-shore range measurements were increased by 10%) and the gas transfer velocities recalculated from equations (5) and (6). Including this potential bias increased the observed quadratic wind speed dependence of the *k* measurements by ~6% (Figure 6). The relationship remained suppressed relative to previous parameterizations, with the ratio of the quadratic fit to the relationship of W14 increased from 0.75 to 0.80.

Instrument failures resulted in pCO_2w measurements only being made from one location in the lead waters, to the E^{loc} of the mast approximately 3 m from the ice floe edge. Horizontal gradients of pCO_2w within the lead waters are a potential source of error in the determination of *k* which may be dependent on relative wind direction and/or fetch. Large gradients would violate the stationarity assumption required for EC and may be removed by the flux quality control procedures. Vertical gradients in pCO_2w above the measurement depth (which would act to reduce ΔpCO_2 and so result in a low bias in the estimate of *k*) are expected to be small due to the persistent wind forcing and shallow measurement depth (0.5 m). The sustained higher winds from September 1 to 5 and on September 8 do not cause large increases in pCO_2w (Figure 3). For the location of the pCO_2w sensor, close to the mast, the winds here were largely off ice, and the waters around the sensor somewhat sheltered with minimal fetch. Hence the mixing and gas transfer in the vicinity of the sensor may have been smaller than in the lead away from the shore. Alternatively, the increased ice growth during these later periods may have suppressed the wind-induced mixing in the lead more generally, resulting in the smaller response of the measured pCO_2w to wind.

4.2 Physical influence

Buoyancy flux was estimated from the heat flux measurements using the COAREG 3.6 algorithm (Edson et al., 2013; Blomquist et al., 2017). Surface cooling conditions resulted in slightly higher *k* measurements (Figure 7a). The buoyancy dependence is smaller than that observed in a shallow lake, close to the Arctic circle in summertime (MacIntyre et al., 2010), and the standard error of the measurements separated by buoyancy overlaps. The *k* dependence on atmospheric stability (determined from measurements as z/L, where z is the measurement height and L is the Obukhov length) was very similar as to buoyancy. During the melt season in the Arctic, surface and atmospheric temperatures are both close to the freezing point of sea water and the measured buoyancy flux was generally small (mean flux into the water -3.4 ± 8.0 W m^{-2}). The small buoyancy flux, relatively high winds and the lack of any wind sheltering around the lead results in a minor role for convective turbulence relative to wind forcing in the lead waters.

Fetch observed during the experiment varied from 40 m to 440 m. For winds above 7 m s^{-1} the fetch varied from 75 m to 410 m. The gas transfer measurements are divided into high and low fetch groups, with the boundary (fetch = 260 m) chosen to ensure approximately equal numbers in each grouping at winds above 7 m s^{-1} (Figure 7b). For winds below 7 m s^{-1}, the standard error of the binned gas transfer velocity from the two fetch groups overlaps. For the higher winds, the greater fetch measurements have higher *k*. The lower fetch measurements have lower *k* by 17%. The observed fetch dependence was robust to the potential bias in the determination of *owf*, with both low and high fetch *k* measurements increased by ~7% when the estimated *owf* error was included (Figure 7b). With short fetch and hence small wave heights, and with the surrounding ice pack suppressing swell, lead waters are more akin to deep, saline lakes than to open ocean waters. Gas transfer rates

674 determined experimentally in lake environments (e.g. Cole & Caraco, 1998; Wanninkhof,
675 1992; MacIntyre et al., 2010) are lower than those observed in the open ocean. However,
676 these measurements are obtained in limited wind speed ranges (below 9 m s^{-1} for the three
677 experiments listed) and the determination of additional forcings has typically focused on
678 factors (e.g. lake-bottom influence) not relevant to the central Arctic Ocean. At the higher
679 winds measured during this experiment (above ~ 9 m s^{-1}), small breaking waves and
680 whitecaps were observed in the lead. The influence of bubble-mediated exchange is not
681 accounted for in parameterizations based on measurements at winds speeds below that
682 required for wave breaking, or in any gas transfer parameterization based on dual-tracer
683 measurement (e.g. Cole & Caraco, 1998; Nightingale et al., 2000). Fetch is determined
684 implicitly from SIC in the sea-ice configuration of the WAGT model (Bigdeli et al., 2018).
685 The fetch-limited configuration of the model, with SIC set to 0, has explicit fetch
686 dependence. In both configurations, the model dependence on fetch and wind speed is weaker
687 than for the observations reported here (Figures 12, 14). The COAREG3.5 physical model
688 (Blomquist et al., 2017) incorporates sea state dependent bubble-mediated gas transfer. The
689 COARE model, with significant wave height determined from the fetch measurements using
690 the relationship of Carter (1982), overestimates the observed gas transfer at wind speeds
691 below ~ 7 m s^{-1} and underestimates at higher wind speeds. The magnitude of the COARE
692 model estimates of fetch dependence is approximately constant with wind speed, higher than
693 relationship observed in the EC measurements at lower wind speeds and a weaker
694 dependence than observed at the higher wind speeds. The COARE algorithm can be tuned to
695 fit observations by modifying two constants that determine molecular sublayer resistance to
696 gas transfer and the dependence on whitecap fraction of bubble-mediated transfer. Here we
697 use values for the constants as determined during high wind conditions in the North Atlantic
698 (A = 1.2, B = 3.8; Blomquist et al., 2017). Adjustments of these constants, as well as further
699 development of the sea state dependence of the transfer coefficients within COARE, may
700 lead to improved agreements between the model and observations reported here.

701

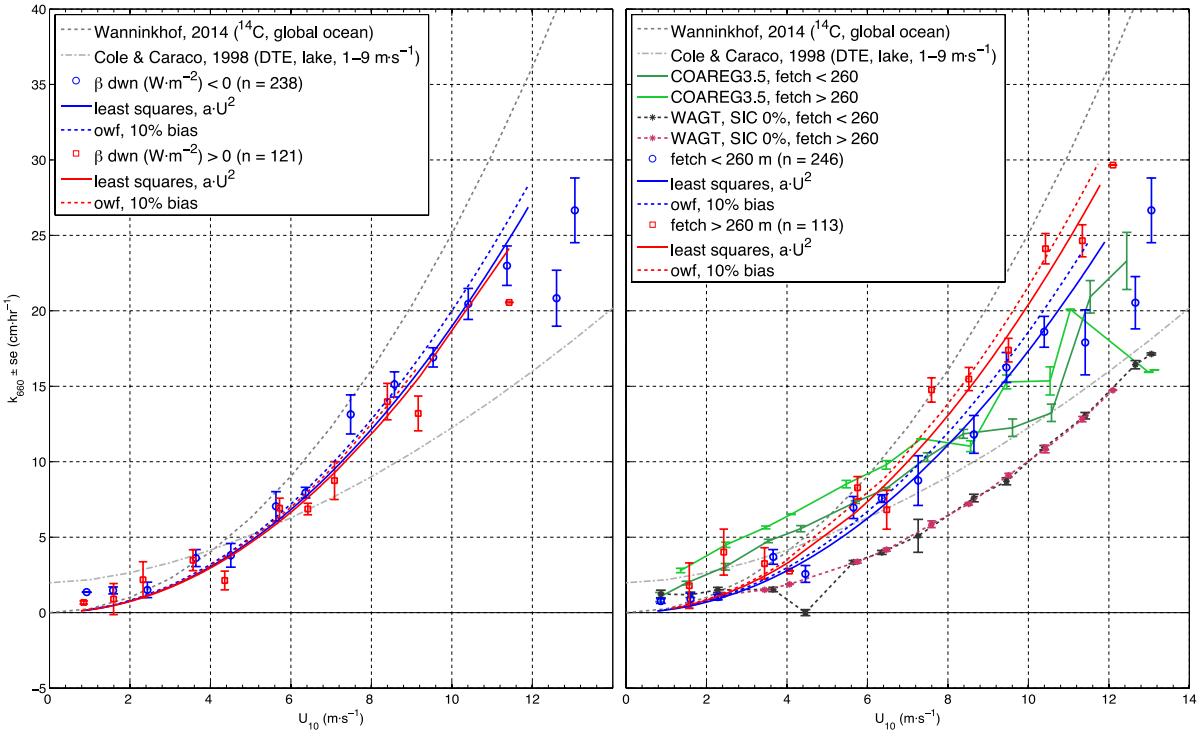

Figure 7. a) Observed dependence of k_{660} on U_{10} and: a) buoyancy flux into the lead water (β), with k_{660} measurements separated into positive (red line) and negative (blue line) buoyancy groupings; b) fetch, with k_{660} separated into high (fetch > 260 m, red line) and low (fetch < 260 m, blue line) groupings. The WAGT and COAREG3.5 model estimates are shown separated into the same fetch groupings as for the measurements. For both a and b, measurements are binned in 1 m s^{-1} wide wind speed bins. The bin center shows the median of the binned measurements and the error bars show the standard error. Least squares quadratic fits are shown for both each grouping for U_{10} < 12 m s^{-1} (solid lines); and with a 10% reduction in measured lead far shore distance (dashed lines). Grey lines show published wind speed parameterizations of k_{660} as listed in the legend with the measurement type, location and wind speed ranges used to derive the parameterization.

5 Conclusions

We report the first direct determination of gas transfer velocities in a sea-ice lead, from ice-based measurements at a lead in the central Arctic Ocean during the transition between summer melt and autumn freeze up seasons. The gas transfer velocities were determined from eddy covariance CO_2 flux measurements made during favourable conditions, i.e. low humidity flux and high ΔpCO_2 conditions. Measurements were made of both lead water – atmosphere and ice/snow –atmosphere fluxes and are the first direct flux measurements reported for pack ice in the summer-autumn season. A flux footprint analysis was used to determine the flux into the lead surface from which the gas transfer velocity was derived.

Measurements were determined for wind speeds up to 13.1 m s^{-1}. The measured k_{660} has a quadratic wind speed dependence, approximately 25% lower than widely used open-

ocean and coastal-ocean parameterisations (e.g. W14; Nightingale et al., 2000) and approximately 30% higher than a commonly used parameterization for gas transfer through lake surfaces (Cole & Caraco, 1998). The measurements exhibit a fetch dependence, demonstrating the importance of lead dimensions and the resulting wave characteristics on gas exchange. Conversely, the measurements exhibit little dependence on convection driven turbulence driven by buoyancy flux, suggesting this is not a significant driver of gas exchange for this location and season.

These results suggest that current methodology for estimating polar air-water carbon exchange, using open ocean gas transfer parameterizations either scaled linearly by open water fraction or enhanced above this scaling, over estimate gas exchange rates. Improved estimates of gas transfer in sea-ice regions will likely require parameterisations that incorporate sea state dependency appropriate for lead scales and the deep, saline ocean conditions. While these observations demonstrate the requirements for parameterization of summer and autumn gas exchange, further observations are required, particularly for the winter season when large heat fluxes from lead surfaces may drive strong convective turbulence. Additional forcings of upper ocean turbulence, such as form drag from ice edges, may have greater impacts on leads of smaller scales than observed here.

Furthermore, scaling such parameterizations to regional gas exchange estimates will require incorporating lead width distributions, as observed with passive (Bröhan and Kaleschke, 2014) and active (Wernecke and Kaleschke, 2015) remote sensing, as well as wind speed and direction relative to lead orientation. Lead widths exhibit a power law distribution (Marq and Weiss, 2012), hence a large fraction of total lead area will consist of leads smaller than that in this study. Direct determinations of gas exchange through such leads likely requires mobile observations with large footprint areas that can integrate varying lead scales (such as from planes and ships; Prytherch et al., 2017).

Data

All micrometeorological and gas exchange data from this project are available on The Bolin Centre Database (https://bolin.su.se/data/ao2018-micromet-icefloe-5). Autonomous sea-ice measurements (snow depth) from August 16 2018 to September 16 2018 were obtained from http://www.meereisportal.de (grant: REKLIM-2013-04).

Acknowledgments

This work is part of the Arctic Ocean 2018 (AO2018) expedition and was funded by The Bolin Centre for Climate Research. The Swedish Polar Research Secretariat (SPRS) provided access to the icebreaker *Oden* and logistical support. The authors are grateful to the Chief Scientists Caroline Leck and Patricia Matrai for planning and coordination of AO2018, and in particular to the SPRS logistical staff and *Oden*'s Captain Mattias Peterson and his crew for their invaluable support. We are also grateful to Prof. Ian Brooks (U. Leeds, UK) for providing instrumentation and invaluable advice.

References

Aijaz, S., W. E. Rogers, and A. V. Babanin (2016), Wave spectral response to sudden changes in wind direction in finite-depth waters, Ocean Modelling, 103, 98–117. doi:10.1016/j.ocemod.2015.11.006

759 Andreas, E. L., T. W., Horst, A. A. Grachev, P. O. G. Persson, C. W. Fairall, C. W., P. S.
760 Guest, and R. E. Jordan (2010), Parameterizing turbulent exchange over summer sea ice
761 and the marginal ice zone, Q, J. R. Meteorol. Soc., 136(649), 927–943.
762 doi:10.1002/qj.618.

763 Bakker, D. C. et al. (2016), A multi-decade record of high quality fCO_2 data in version 3 of
764 the Surface Ocean CO_2 Atlas (SOCAT), Earth System Science Data, 8, 383-
765 413. doi:10.5194/essd-8-383-2016.

766 Bates, N. R., and J. T. Mathis (2009), The Arctic Ocean marine carbon cycle: Evaluation of
767 air-sea CO_2 exchanges, ocean acidification impacts and potential feedbacks,
768 Biogeosciences, 6(11), 2433–2459.

769 Bariteau, L., D. Helmig, C. W. Fairall, J. E. Hare, J. Hueber, and E. K. Lang (2010),
770 Determination of oceanic ozone deposition by ship-borne eddy covariance flux
771 measurements, Atmos. Meas. Tech., 3(2), 441–455. doi:10.5194/amt-3-441-2010.

772 Bigdeli, A., T. Hara, B. Loose, and A. T. Nguyen (2018), Wave attenuation and gas exchange
773 velocity in marginal sea ice zone. J. Geophys. Res.-Oceans, 123, 2293–2304,
774 doi:10.1002/2017JC013380.

775 Blomquist, B. W., B, J. Huebert, C. W. Fairall, L. Bariteau, J. B. Edson, J. E. Hare, and W. R.
776 McGillis (2014), Advances in air-sea CO_2 flux measurement by eddy correlation,
777 Boundary Layer Meteorol., 152(3), 245–276, doi:10.1007/s10546-014-9926-2.

778 Blomquist, B. W., S. E. Brumer, C. W. Fairall, B. J. Huebert, C, J. Zappa, I. M. Brooks, M.
779 Yang, L. Bariteau, J. Prytherch, J. E. Hare, H. Czerski, A. Matei, and R. W. Pascal (2017),
780 Wind Speed and Sea State Dependencies of Air- Sea Gas Transfer: Results From the High
781 Wind Speed Gas Exchange Study (HiWinGS), J. Geophys. Res.-Oceans, 122(10), 8034–
782 8062. doi:10.1002/2017jc013181.

783 Bowling, D. R., and W. J. Massman (2011), Persistent wind-induced enhancement of
784 diffusive CO_2 transport in a mountain forest snowpack, J. Geophys. Res., 116(G4),
785 doi:10.1029/2011jg001722.

786 Bröhan, D., and L. Kaleschke (2014), A Nine-Year Climatology of Arctic Sea Ice Lead
787 Orientation and Frequency from AMSR-E, Remote Sens., 6(2), 1451–1475.
788 doi:10.3390/rs6021451.

789 Brumer, S. E., C. J. Zappa, B. Blomquist, C. W. Fairall, A. Cifuentes-Lorenzen, J. B. Edson,
790 I. M. Brooks, and B. Huebert (2017), Wave-related Reynolds number parameterizations of
791 CO_2 and DMS transfer velocities, Geophys. Res. Letts., 44. doi:10.1002/2017GL074979.

792 Burba, G. G., D. K. McDermitt, A. Grelle, D. J. Anderson, and L. Xu (2008), Addressing the
793 influence of instrument surface heat exchange on the measurements of CO_2 flux from
794 open-path gas analyzers, Global Change Biol., 14(8), 1854–1876. doi:10.1111/j.1365-
795 2486.2008.01606.x.

796 Butterworth, B, J., and B. G. T. Else (2018), Dried, closed-path eddy covariance method for
797 measuring carbon dioxide flux over sea ice, Atmos. Meas. Tech., 11(11), 6075–6090.
798 doi:10.5194/amt-11-6075-2018.

799 Butterworth, B, J., and S. D. Miller (2016a), Air-sea exchange of carbon dioxide in the
800 Southern Ocean and Antarctic marginal ice zone, Geophys. Res. Lett., 43, 7223–7723,
801 doi:10.1002/2016GL069581.

Butterworth, B. J., and S. D. Miller (2016b), Automated underway eddy covariance system for air-sea momentum, heat, and CO_2 fluxes in the Southern Ocean, J. Atmos. Ocean. Technol., 33(4), 635–652, doi:10.1175/JTECH-D-15-0156.1.

Carter, D, J. T. (1982), Prediction of wave height and period for a constant wind velocity using the JONSWAP results, Ocean Eng, 9(1), 17–33. doi:10.1016/0029-8018(82)90042-7.

Chen, D. D., C. S.Ruf, and S. T. Gleason (2016), Response time of mean square slope to wind forcing: An empirical investigation, J. Geophys. Res.-Oceans, 121(4), 2809–2823. doi:10.1002/2016jc011661.

Cole, J. J., and N. F. Caraco (1998), Atmospheric exchange of carbon dioxide in a low-wind oligotrophic lake measured by the addition of SF_6, Limnol. Oceanogr., 43(4), 647–656. doi:10.4319/lo.1998.43.4.0647.

Delille, B., et al. (2014), Southern Ocean CO_2 sink: The contribution of the sea ice, J. Geophys. Res.-Oceans, 119, 6340–6355, doi:10.1002/2014JC009941.

Edson, J. B., C. W. Fairall, L. Bariteau, C. J. Zappa, A. Cifuentes-Lorenzen, W. R. McGillis, S. Pezoa, J. E. Hare, and D. Helmig (2011), Direct covariance measurement of CO_2 gas transfer velocity during the 2008 Southern Ocean Gas Exchange Experiment: Wind speed dependency, J. Geophys. Res., 116. doi:10.1029/2011jc007022.

Edson, J. B., V. Jampana, R. A. Weller, S. P. Bigorre, A. J. Plueddemann, C, W. Fairall, S. D. Miller, L. Mahrt, D. Vickers, and H. Hersbach, (2013), On the Exchange of Momentum over the Open Ocean, J. Phys. Oceanogr., 43(8), 1589–1610. doi:10.1175/jpo-d-12-0173.1.

Else, B. G. T., T. N. Papakyriakou, R, J. Galley, W. M. Drennan, L. A. Miller, and H. Thomas (2011), Wintertime CO2 fluxes in an Arctic polynya using eddy covariance: Evidence for enhanced air-sea gas transfer during ice formation, J. Geophys. Res., 116, C00G03, doi:10.1029/2010JC006760.

Fanning, K. A., and L. M. Torres (1991), 222Rn and 226Ra: Indicators of sea-ice effects on air-sea gas exchange, Polar Res., 10(1), 51–58.

Foken, T., and B. Wichura (1996), Tools for quality assessment of surface-based flux measurements, Agric. For. Meteorol., 78(1), 83–105, doi:10.1016/0168-1923(95)02248-1.

Geilfus, N. X., G. Carnat, T. Papakyriakou, J. L. Tison, B. Else, H. Thomas, E. Shadwick, and B. Delille (2012), Dynamics of pCO2 and related air-ice CO2 fluxes in the Arctic coastal zone (Amundsen Gulf, Beaufort Sea), J. Geophys. Res., 117, C00G10, doi:10.1029/2011JC007118.

Geilfus, N. X., R, J. Galley, O. Crabeck, T. Papakyriakou, J. Landy, J. L. Tison, and S. Rysgaard (2015), Inorganic carbon dynamics of melt-pond-covered first-year sea ice in the Canadian Arctic, Biogeosciences, 12(6), 2047–2061, doi:10.5194/bg-12-2047-2015.

Gosink, T. A., J. G. Pearson, and J. J. Kelley (1976), Gas movement through sea ice, Nature, 263(5572), 41–42. doi:10.1038/263041a0.

Hignett, P. (1998), Correction of airborne SST measurements for blackness effects, MRF Tech. Note 28, 15 pp., Meteorol. Res. Flight, Hampshire, England.

Ho, D. T., C. S. Law, M, J. Smith, P. Schlosser, M. Harvey, and P. Hill (2006), Measurements of air- sea gas exchange at high wind speeds in the Southern Ocean:

Implications for global parameterizations, Geophys. Res. Lett., 33, L16611, doi:10.1029/2006GL026817.

Honkanen, M., J.–P. Tuovinen, T. Laurila, T. Mäkelä, J. Hatakka, S. Kielosto, and L. Laakso (2018), Measuring turbulent CO_2 fluxes with a closed-path gas analyzer in a marine environment. Atmos. Meas. Tech., 11(9), 5335–5350, doi:10.5194/amt-11-5335-2018.

Horst, T. W. (1997), A simple formula for attenuation of eddy fluxes measured with first-order-response scalar sensors, Boundary Layer Meteorol., 82(2), 219–233. doi:10.1023/a:1000229130034.

Jähne, B., K. O. Münnich, R. Bösinger, A. Dutzi, W. Huber, and P. Libner (1987), On the parameters influencing air-water gas exchange, J. Geophys. Res., 92, 1937–1949, doi:10.1029/JC092iC02p01937.

Kaimal, J. C., Y. Izumi, J. C. Wyngaard, and R. Cote (1972), Spectral characteristics of surface- layer turbulence, Q, J. R. Meteorol. Soc., 98(417), 563–589, doi:10.1002/qj.49709841707.

Kljun, N., P. Calanca, M. W. Rotach, and H. P. Schmid (2015), A simple two-dimensional parameterisation for Flux Footprint Prediction (FFP), Geosci. Model Dev., 8(11), 3695–3713. doi:10.5194/gmd-8-3695-2015.

Landwehr, S., S. D. Miller, M, J. Smith, E. S. Saltzman, and B. Ward (2014), Analysis of the PKT correction for direct CO_2 flux measurements over the ocean, Atmos. Chem. Phys., 14(7), 3361–3372, doi:10.5194/acp-14-3361-2014.

Loose, B., W. R. McGillis, P. Schlosser, D. Perovich, and T. Takahashi (2009), Effects of freezing, growth, and ice cover on gas transport processes in laboratory seawater experiments, Geophys. Res. Lett., 36, L05603, doi:10.1029/2008GL036318.

Loose, B., W. R. McGillis, D. Perovich, C, J. Zappa, and P. Schlosser (2014), A parameter model of gas exchange for the seasonal sea ice zone, Ocean Sci., 10, 17–28, doi:10.5194/os-10-17-2014.

Loose, B., R. P. Kelly, A. Bigdeli, W. Williams, R. Krishfield, M. Rutgers van der Loeff, and S. B. Moran (2017), How well does wind speed predict air-sea gas transfer in the sea ice zone? A synthesis of radon deficit profiles in the upper water column of the Arctic Ocean, J. Geophys. Res.-Oceans, 122(5), 3696–3714. doi:10.1002/2016jc012460.

Lovely, A., B. Loose, P. Schlosser, W. McGillis, C. Zappa, D. Perovich, S. Brown, T. Morell, D. Hsueh, and R. Friedrich (2015), The Gas Transfer through Polar Sea ice experiment: Insights into the rates and pathways that determine geochemical fluxes, J. Geophys. Res.-Oceans, 120, 8177–8194, doi:10.1002/2014JC010607.

Lüpkes, C., V. M. Gryanik, J. Hartmann, and E. L. Andreas (2012), A parameterization, based on sea ice morphology, of the neutral atmospheric drag coefficients for weather prediction and climate models, J. Geophys. Res.-Atmos., 117(D13), n/a-n/a. doi:10.1029/2012jd017630.

MacGilchrist, G. A., A. C. Naveira Garabato, T. Tsubouchi, S. Bacon, S. Torres-Valdés, and K. Azetsu-Scott (2014), The Arctic Ocean carbon sink, Deep Sea Res., Part. I, 86, 39–55. doi:10.1016/j.dsr.2014.01.002

MacIntyre, S., A. Jonsson, M. Jansson, J. Aberg, D. E. Turney, and S. D. Miller (2010), Buoyancy flux, turbulence, and the gas transfer coefficient in a stratified lake, Geophys. Res. Lett., 37(24), n/a-n/a. doi:10.1029/2010gl044164.

Marcq, S., and J. Weiss (2012), Influence of sea ice lead-width distribution on turbulent heat transfer between the ocean and the atmosphere, The Cryosphere, 6(1), 143–156. doi:10.5194/tc-6-143-2012.

Massman, W, J. and R. Clement (2004), Uncertainty in eddy covariance flux estimates resulting from spectral attenuation, in: Handbook of Micrometeorology, A Guide for Surface Flux Measurement and Analysis, edited by: Lee, X., Massman, W, J., and Law, B. E., Kluwer, 67–99.

McGillis, W. R., J. B. Edson, J. E. Hare, and C. W. Fairall (2001), Direct covariance air-sea CO_2 fluxes, J. Geophys. Res., 106, 16,729–16,745, doi:10.1029/2000JC000506.

McKenna, S. P. and W. R. McGillis (2004), The role of free-surface turbulence and surfactants in air-water gas transfer, Int, J. Heat Mass Transf. **47**, 539–553.

Miller, L. A., G. Carnat, B. G. T. Else, N. Sutherland, and T. N. Papakyriakou (2011a), Carbonate system evolution at the Arctic Ocean surface during autumn freeze-up, J. Geophys. Res., 116. doi:10.1029/2011jc007143.

Miller, L. A., T. N. Papakyriakou, R. E. Collins, J. W. Deming, J. K. Ehn, R. W. Macdonald, A. Mucci, O. Owens, M. Raudsepp, and N. Sutherland (2011b), Carbon dynamics in sea ice: A winter flux time series, J. Geophys. Res., 116, C02028, doi:10.1029/2009JC006058.

Miller, S. D., C. Marandino, and E. S. Saltzman (2010), Ship-based measurement of air-sea CO_2 exchange by eddy covariance, J. Geophys. Res., 115, D02304, doi:10.1029/2009JD012193.

Miller, S. D., M. L. Goulden, M. C. Menton, H. R. da Rocha, H. C. de Freitas, A. M. e S. Figueira, and C. A. Dias de Sousa, (2004), Biometric and micrometeorological measurements of tropical forest carbon balance, Ecol. Appl., 14(sp4), 114–126. doi:10.1890/02-6005.

Miller, L. A., F. Fripiat, B. G. T. Else, J. S. Bowman, K. A. Brown, R. E. Collins, M. Ewert, A. Fransson, M. Gosselin, D. Lannuzel, K. M. Meiners, C. Michel, J. Nishioka, D. Nomura, S. Papadimitriou, L. M. Russell, L. L. Sorensen, D. N. Thomas, J-L. Tison, M. A. van Leeuwe, M. Vancoppenolle, E. W. Wolff, and J. Zhou (2015), Methods for biogeochemical studies of sea ice: The state of the art, caveats, and recommendations, Elementa: Sci. Anthropocene, 3, 38. doi:10.12952/journal.elementa.000038.

Moncrieff, J. B., J. M. Massheder, H. de Bruin, J. Elbers, T. Friborg, B. Heusinkveld, P. Kabat, S. Scott, H. Soegaard, and A. Verhoef (1997), A system to measure surface fluxes of momentum, sensible heat, water vapour and carbon dioxide, J. Hydrol., 188–189, 589–611. doi:10.1016/s0022-1694(96)03194-0.

Nightingale, P. D., G. Malin, C. S. Law, A, J. Watson, P. S. Liss, M. I. Liddicoat, J. Boutin, and R. C. Upstill- Goddard (2000), In situ evaluation of air- sea gas exchange parameterizations using novel conservative and volatile tracers, Global Biogeochem. Cycles, 14, 373–387, doi:10.1029/1999GB900091.

Nomura, D., M. A. Granskog, P. Assmy, D. Simizu, and G. Hashida (2013), Arctic and Antarctic sea ice acts as a sink for atmospheric CO_2 during periods of snowmelt and surface flooding, J. Geophys. Res.-Oceans, 118, 6511–6524, doi:10.1002/2013JC009048.

Nomura, D., H. Yoshikawa-Inoue, T. Toyota, and K. Shirasawa (2010), Effects of snow, snow melting and refreezing processes on air–sea-ice CO_2 flux, J. Glaciol., 56(196), 262–270. doi:10.3189/002214310791968548.

Nomura, D., M. A. Granskog, A. Fransson, M. Chierici, A. Silyakova, K. I. Ohshima, L. Cohen, B. Delille, S. R. Hudson, and G. S. Dieckmann, (2018), CO_2 flux over young and snow-covered Arctic pack ice in winter and spring, Biogeosciences, 15(11), 3331–3343. doi:10.5194/bg-15-3331-2018.

Persson, P. O. G., J. E. Hare, C. W. Fairall, and W. D. Otto (2005), Air–sea interaction processes in warm and cold sectors of extratropical cyclonic storms observed during FASTEX, Q, J. R. Meteorol. Soc., 131(607), 877–912. doi:10.1256/qj.03.181.

Prytherch, J., I. M. Brooks, P. M. Crill, B. F. Thornton, D, J. Salisbury, M. Tjernström, L. G. Anderson, M. C. Geibel, and C. Humborg (2017), Direct determination of the air-sea CO_2 gas transfer velocity in Arctic sea ice regions, Geophys. Res. Lett., 44, 3770–3778, doi:10.1002/2017GL073593.

Prytherch, J., M. J. Yelland, I. M. Brooks, D. J. Tupman, R. W. Pascal, B. I. Moat, and S. J. Norris (2015), Motion-correlated flow distortion and wave-induced biases in air-sea flux measurements from ships, Atmos. Chem. Phys., 15(18), 10,619–10,629, doi:10.5194/acp-15-10619-2015.

Prytherch, J., M, J. Yelland, R. W. Pascal, B. I. Moat, I. Skjelvan, and C. C. Neill (2010), Direct measurements of the CO_2 flux over the ocean: Development of a novel method, Geophys. Res. Lett., 37, L03607, doi:10.1029/2009GL041482.

Read, J. S., D. P. Hamilton, A. R. Desai, K. C. Rose, S. MacIntyre, J. D. Lenters, R. L. Smyth, P. C. Hanson, J. J. Cole, P. A. Staehr, J. A., Rusak, D. C. Pierson, J. D. Brookes, A. Laas, and C. H. Wu (2012), Lake-size dependency of wind shear and convection as controls on gas exchange, Geophys. Res. Lett., 39(9), n/a-n/a. doi:10.1029/2012gl051886.

Rutgers van der Loeff, M. M., N. Cassar, M. Nicolaus, B. Rabe, and I. Stimac (2014), The influence of sea ice cover on air-sea gas exchange estimated with radon-222 profiles, J. Geophys. Res.-Oceans, 119, 2735–2751, doi:10.1002/2013JC009321.

Sabbaghzadeh, B., R. C. Upstill-Goddard, R. Beale, R. Pereira, and P. D. Nightingale (2017), The Atlantic Ocean surface microlayer from 50°N to 50°S is ubiquitously enriched in surfactants at wind speeds up to 13m s^{-1}, Geophys. Res. Lett., 44, 2852–2858, doi:10.1002/2017GL072988.

Salter, M. E., R. C. Upstill-Goddard, P. D. Nightingale, S. D. Archer, B. Blomquist, D. T. Ho, B. Huebert, P. Schlosser, and M. Yang (2011), Impact of an artificial surfactant release on air-sea gas fluxes during Deep Ocean Gas Exchange Experiment II, J. Geophys. Res., 116(C11), doi:10.1029/2011jc007023.

Sievers, J., L. L. Sørensen, T. Papakyriakou, B. Else, M. K. Sejr, D. Haubjerg Søgaard, D. Barber, and S. Rysgaard (2015), Winter observations of CO_2 exchange between sea ice and the atmosphere in a coastal fjord environment, Cryosphere, 9(4), 1701–1713, doi:10.5194/tc-9- 1701-2015.

Smith, S. (1988), Coefficients for sea surface wind stress, heat flux, and wind profiles as a function of wind speed and temperature, J. Geophys. Res., 93, 15,467–15,472, doi:10.1029/JC093iC12p15467.

Spirig, C., A. Neftel, C. Ammann, J. Dommen, W. Grabmer, A. Thielmann, A. Schaub, J. Beauchamp, A. Wisthaler, and A. Hansel (2005), Eddy covariance flux measurements of biogenic VOCs during ECHO 2003 using proton transfer reaction mass spectrometry, Atmos. Chem. Phys., 5(2), 465–481. doi:10.5194/acp-5-465-2005.

978 Spreen, G., L. Kaleschke, and G. Heygster (2008), Sea ice remote sensing using AMSR-E
979 89-GHz channels, J. Geophys. Res., 113, C02S03, doi:10.1029/2005JC003384.

980 Takagi, K., M. Nomura, D. Ashiya, H. Takahashi, K. Sasa, Y. Fujinuma, H. Shibata, Y.
981 Akibayashi, and T. Koike (2005), Dynamic carbon dioxide exchange through snowpack
982 by wind-driven mass transfer in a conifer-broadleaf mixed forest in northernmost Japan,
983 Global Biogeochem. Cy., 19(2), n/a-n/a. doi:10.1029/2004gb002272.

984 Takahashi, T., et al. (2009), Climatological mean and decadal change in surface ocean pCO_2,
985 and net sea–air CO_2 flux over the global oceans, Deep Sea Res., Part. II, 56(8), 554–577,
986 doi:10.1016/j.dsr2.2008.12.009.

987 Tjernström, M., C. E. Birch, I. M. Brooks, M. D. Shupe, P. O. G. Persson, J. Sedlar, T.
988 Mauritsen, C. Leck, J. Paatero, M. Szczodrak, and C. R. Wheeler (2012), Meteorological
989 conditions in the central Arctic summer during the Arctic Summer Cloud Ocean Study
990 (ASCOS), Atmos. Chem. Phys., 12(15), 6863–6889. doi:10.5194/acp-12-6863-2012.

991 Vachon, D., and Y. T. Prairie (2013), The ecosystem size and shape dependence of gas
992 transfer velocity versus wind speed relationships in lakes, Can. J. Fish. Aquat. Sci.,
993 70(12), 1757–1764. doi:10.1139/cjfas-2013-0241.

994 van Dijk et al. 2004: The principles of surface flux physics: theory, practice and description
995 of the ECPACK library (www.met.wau.nl/projects/jep).

996 Vickers, D., and L. Mahrt (1997), Quality Control and Flux Sampling Problems for Tower
997 and Aircraft Data, J. Atmos. Ocean. Technol., 14(3), 512–526. doi:10.1175/1520-
998 0426(1997)014<0512:qcafsp>2.0.co;2.

999 Wanninkhof, R. (1992), Relationship between wind speed and gas exchange over the ocean,
1000 J. Geophys. Res., 97(C5), 7373. doi:10.1029/92jc00188.

1001 Wanninkhof, R., W. E. Asher, D. T. Ho, C. Sweeney, and W. R. McGillis (2009), Advances
1002 in quantifying air-sea gas exchange and environmental forcing, Annu. Rev. Mar. Sci., 1,
1003 213–244, doi:10.1146/annurev.marine.010908.163742.

1004 Wanninkhof, R. (2014), Relationship between wind speed and gas exchange over the ocean
1005 revisited, Limnol. Oceanogr. Meth., 12(6), 351–362, doi:10.4319/lom.2014.12.351.

1006 Webb, E. K., G. I. Pearman, and R. Leuning (1980), Correction of flux measurements for
1007 density effects due to heat and water vapour transfer, Q, J. R. Meteorol. Soc., 106(447),
1008 85–100, doi:10.1002/qj.49710644707.

1009 Weiss, R. (1974), Carbon dioxide in water and seawater: The solubility of a non-ideal gas,
1010 Mar. Chem., 2(3), 203–215, doi:10.1016/0304-4203 (74)90015-2.

1011 Wernecke, A., and L. Kaleschke (2015), Lead detection in Arctic sea ice from CryoSat-2:
1012 quality assessment, lead area fraction and width distribution, The Cryosphere, 9(5), 1955–
1013 1968. doi:10.5194/tc-9-1955-2015.

1014 Wilczak, J. M., S. P. Oncley, and S. A. Stage (2001), Sonic Anemometer Tilt Correction
1015 Algorithms, Boundary Layer Meteorol., 99(1), 127–150. doi:10.1023/a:1018966204465.

1016 Woolf, D. K. (2005), Parameterization of gas transfer velocities and sea- state- dependent
1017 wave breaking, Tellus, Ser. B, 57, 87–94, doi:10.1111/j.1600-0889.2005.00139.x.

1018 Woolf, D. K., J. D. Shutler, L. Goddijn- Murphy, A. J. Watson, B. Chapron, P. D.
1019 Nightingale, C. J. Donlon, J. Piskozub, M. J. Yelland, I. Ashton, T. Holding, U. Schuster,
1020 F. Girard- Ardhuin, A. Grouazel, J-F. Piolle, M. Warren, I. Wrobel- Niedzwiecka, P. E.

1021 Land, R. Torres, J. Prytherch, B. Moat, J. Hanafin, F. Ardhuin, and F. Paul (2019), Key
1022 Uncertainties in the Recent Air- Sea Flux of CO_2, Global Biogeochem. Cycles, 33(12),
1023 1548–1563. doi:10.1029/2018gb006041.

1024 Yang, M., J. Prytherch, E. Kozlova, M, J. Yelland, D. Parenkat Mony, and T. G. Bell (2016),
1025 Comparison of two closed-path cavity-based spectrometers for measuring air-water CO_2
1026 and CH_4 fluxes by eddy covariance, Atmos. Meas. Tech., 9(11), 5509–5522,
1027 doi:10.5194/amt- 9-5509-2016.

1028 Yasunaka, S., E. Siswanto, A. Olsen, M. Hoppema, E. Watanabe, A. Fransson, M. Chierici,
1029 A. Murata, S. K. Lauvset, R. Wanninkhof, T. Takahashi, N. Kosugi, A. M. Omar, S. van
1030 Heuven, and J. T. Mathis (2018), Arctic Ocean CO_2 uptake: An improved multiyear
1031 estimate of the air-sea CO_2 flux incorporating chlorophyll a concentrations.
1032 Biogeosciences, 15(6), 1643–1661, doi:10.5194/bg-15-1643-2018.

1033 Yelland, M. J., B. I. Moat, R. W. Pascal, and D. I. Berry (2002), CFD model estimates of the
1034 airflow distortion over research ships and the impact on momentum flux measurements, J.
1035 Atmos. Ocean. Technol., 19, 1477–1499, doi:10.1175/1520-
1036 0426(2002)019<1477:CMEOTA>2.0.CO;2.

1037 Zippel, S., and J. Thomson (2016), Air-sea interactions in the marginal ice zone, Elementa:
1038 Sci. Anthropocene, 4(1), 95, doi:10.12952/journal.elementa.000095.